AD__________________

Award Number: DAMD17-03-1-0405

TITLE: Three Dimensional Reconstruction Algorithm for Imaging Pathophysiological Signal within Breast Tissue Using Near Infrared Light

PRINCIPAL INVESTIGATOR: Hamid Dehghani, Ph.D.

CONTRACTING ORGANIZATION: Dartmouth College
Hanover, NH 03755-1404

REPORT DATE: July 2004

TYPE OF REPORT: Annual Summary

PREPARED FOR: U.S. Army Medical Research and Materiel Command
Fort Detrick, Maryland 21702-5012

DISTRIBUTION STATEMENT: Approved for Public Release;
Distribution Unlimited

The views, opinions and/or findings contained in this report are those of the author(s) and should not be construed as an official Department of the Army position, policy or decision unless so designated by other documentation.

20050113 079

BEST AVAILABLE COPY

REPORT DOCUMENTATION PAGE

Form Approved
OMB No. 074-0188

Public reporting burden for this collection of information is estimated to average 1 hour per response, including the time for reviewing instructions, searching existing data sources, gathering and maintaining the data needed, and completing and reviewing this collection of information. Send comments regarding this burden estimate or any other aspect of this collection of information, including suggestions for reducing this burden to Washington Headquarters Services, Directorate for Information Operations and Reports, 1215 Jefferson Davis Highway, Suite 1204, Arlington, VA 22202-4302, and to the Office of Management and Budget, Paperwork Reduction Project (0704-0188), Washington, DC 20503

1. AGENCY USE ONLY (Leave blank)	**2. REPORT DATE** July 2004	**3. REPORT TYPE AND DATES COVERED** Annual Summary(15 Jun 2003 - 14 Jun 2004)

4. TITLE AND SUBTITLE
Three Dimensional Reconstruction Algorithm for Imaging Pathophysiological Signal within Breast Tissue Using Near Infrared Light

5. FUNDING NUMBERS
DAMD17-03-1-0405

6. AUTHOR(S)

Hamid Dehghani, Ph.D.

7. PERFORMING ORGANIZATION NAME(S) AND ADDRESS(ES)
Dartmouth College
Hanover, NH 03755-1404

E-Mail: hamid.Dehghani@dartmouth.edu

8. PERFORMING ORGANIZATION REPORT NUMBER

9. SPONSORING / MONITORING AGENCY NAME(S) AND ADDRESS(ES)
U.S. Army Medical Research and Materiel Command
Fort Detrick, Maryland 21702-5012

10. SPONSORING / MONITORING AGENCY REPORT NUMBER

11. SUPPLEMENTARY NOTES

12a. DISTRIBUTION / AVAILABILITY STATEMENT
Approved for Public Release; Distribution Unlimited

12b. DISTRIBUTION CODE

13. ABSTRACT (Maximum 200 Words)

Optical tomography is a non-invasive imaging technique that can image properties of biological tissue. Measurements of light propagation through tissue can be used to calculate and reconstruct images of internal optical properties. Since the absorption and scattering of light in the tissue is a function its physiological state, the aim is to calculate maps of physiological parameters, which can be early markers of tumor development. Specifically the aim is to image total hemoglobin, oxygen saturation, water and lipid concentrations, as well as potentionally molecular concentrations when used with fluorescent markers. Cancerous regions within the breast have shown to be physiologically different from normal tissue. These include a higher amount of angiogenesis and higher metabolic rate as compared to normal tissue. These differences will result in a change in optical attenuation and scatter of light due to hemoglobin changes, which will cause a change in the measured tomographic boundary data. Light transport modeling of propagation in tissue can be used to calculate maps of optical changes within the breast, and therefore physiological maps of total hemoglobin and oxygen saturation.

14. SUBJECT TERMS

Breast Cancer

15. NUMBER OF PAGES
56

16. PRICE CODE

17. SEURITY CLASSIFICATION OF REPORT Unclassified	**18. SECURITY CLASSIFICATION OF THIS PAGE** Unclassified	**19. SECURITY CLASSIFICATION OF ABSTRACT** Unclassified	**20. LIMITATION OF ABSTRACT** Unlimited

NSN 7540-01-280-5500

Standard Form 298 (Rev. 2-89)
Prescribed by ANSI Std. Z39-18
298-102

Table of Contents

Cover……………………………………………………………………1

SF 298……………………………………………………………………2

Introduction……………………………………………………………4

Body……………………………………………………………………4

Key Research Accomplishments………………………………………4

Reportable Outcomes…………………………………………………4

Conclusions……………………………………………………………8

References……………………………………………………………8

Appendices……………………………………………………………8

Introduction

In this work, a novel imaging technique is explored that uses non-harmful application of near infrared light to determine the properties of tissue. Using this technique, known as near infrared (NIR) tomography, an optical fiber placed on the surface of the region of interest, the breast, delivers an input signal while other optical fibers placed at different locations on the same surface detect the outcoming photons, which have propagated through the volume under investigation. The intensity and path-length distributions of the exiting light provide information about the optical properties of the transilluminated tissue using a model-based interpretation where photon propagation is simulated by the diffusion theory. Through iterative solution to match the theory to the real measurements, images of internal absorption and scattering coefficient distribution can be reconstructed. Tissue optical properties have shown to be a function of their structure and more importantly, their physiological state. It is these qualities that provide an alternative method for the detection and characterization of tumor within breast tissue. An important aspect for the success and accuracy of this method is the use of adequate modeling of light within breast tissue. In this work, we have used a Finite Element Model of the Diffusion Approximation, to calculate and predict light transport. Using such technique, we are able to determine, to some accuracy, the distribution of internal optical properties of the tissue under investigation. A major limitation in the development of near infrared imaging so far has been the lack of accurate and fast model-based reconstruction algorithm for this modality.

Body

Since the award of this project, the aims have not changed. In brief these are:(1) Validate, improve and accelerate a three-dimensional finite element model of light propagation within the breast tissue as well as the image reconstruction algorithm for simultaneously calculating the internal absorption and scattering coefficients. (2) Investigate the benefits and limits of using a-priori information from dual modality images, for example, MRI and Near Infrared data. (3) Explore the benefits and limits of using Fluorescent contrast-agents, which will target specific molecular markers of the tumor, giving rise to a-priori information regarding tumor location as well as physiological function of the tissue. (4) Test the developed algorithm on patient data and compare results with available mammograms and biopsy results to evaluate algorithm accuracy

Key research accomplishments

In the initial 12 months of the project, much has been achieved. Namely, (a) Three-dimensional reconstructed images of patient data have been achieved, (b) new image reconstruction algorithms have been developed and (c) initial work has begun in the evaluation of incorporating a-priori information from MRI into NIR image reconstruction.

Reportable outcomes

Preliminary Clinical Results of Frequency Domain DOT

Here, we present sample reconstructed images of internal absorption and scatter from 2 sets of exams where data was collected at multiple wavelengths, ranging from 761 nm to 826 nm on volunteers recruited at Dartmouth-Hitchcock Medical Center. The NIR imaging system hardware, developed by the research team at Dartmouth, is shown in Figure 1. The subject lies flat on the measurement bed Figure 1(a), which contains a single opening for the breast. The breast is suspended freely through this opening and the optical fibers, Figure 1(b), are brought into contact with the breast Figure 2. The optical fiber arrangement consists of a total of 48 fibers, 16 fibers in 3 separate planes. Within each plane the fibers are arranged equidistantly (each separate plane is 10 mm apart from one another in the z direction). The fibers need to make full contact with the breast for high quality NIR measurements.

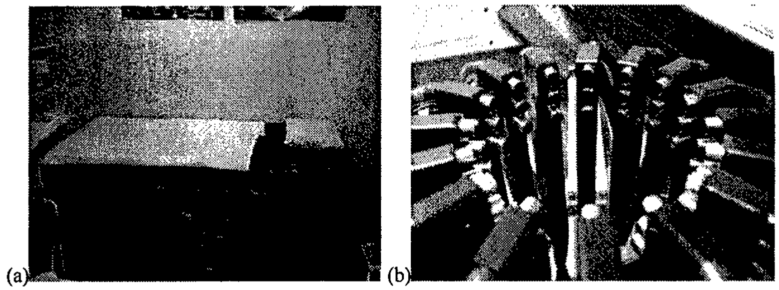

Figure 1. (a) The exam station with a single opening for the breast. (b) Optical fiber probe arrangement (16 equally spaced fibers at 3 separate levels, each level is separated by 10 mm) currently at use. The fibers can be opened or closed to suit each individual subject during setup. The breast is suspended through this opening, and optical fiber probes are brought into contact with the tissue surface.

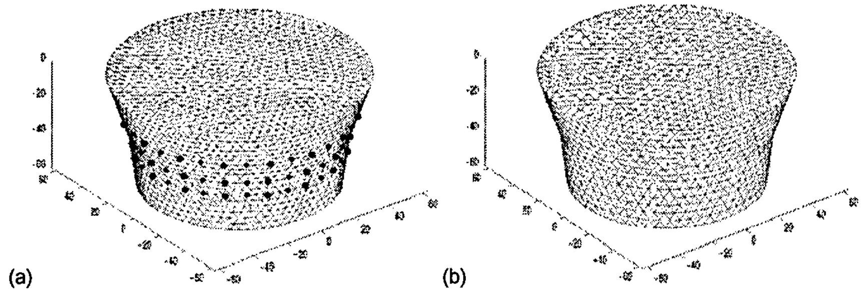

Figure 2. Example of a mesh used for the reconstruction of images from measured clinical data. The information about data collection geometry that was used for mesh generation included slice diameter, allowing generation of: (a) a conical shaped mesh used for light field calculation; (b) a conical shaped mesh used for the reconstruction basis.

For the NIR exams, an attendant translates the fiber optic probes into direct contact with the breast at the level of the clinical abnormality. We obtained three tomographic acquisitions centered on the region of interest, with contiguous slices above and below the primary plane of the abnormality. Measurements collected from a cylindrical phantom at each wavelength were also recorded for calibration purposes. From knowledge of the diameter of each measurement plane and of the separation between planes, we constructed a conical shaped mesh, Figure 2(a). For image reconstruction, each data set was calibrated for each wavelength according to procedures described elsewhere. For the reconstruction basis a second mesh of the same geometry was used, Figure 2(b). The reconstruction time after the initial calibration procedure was approximately 10 min per iteration on a 1.7-GHz PC with 2 Gigs of RAM

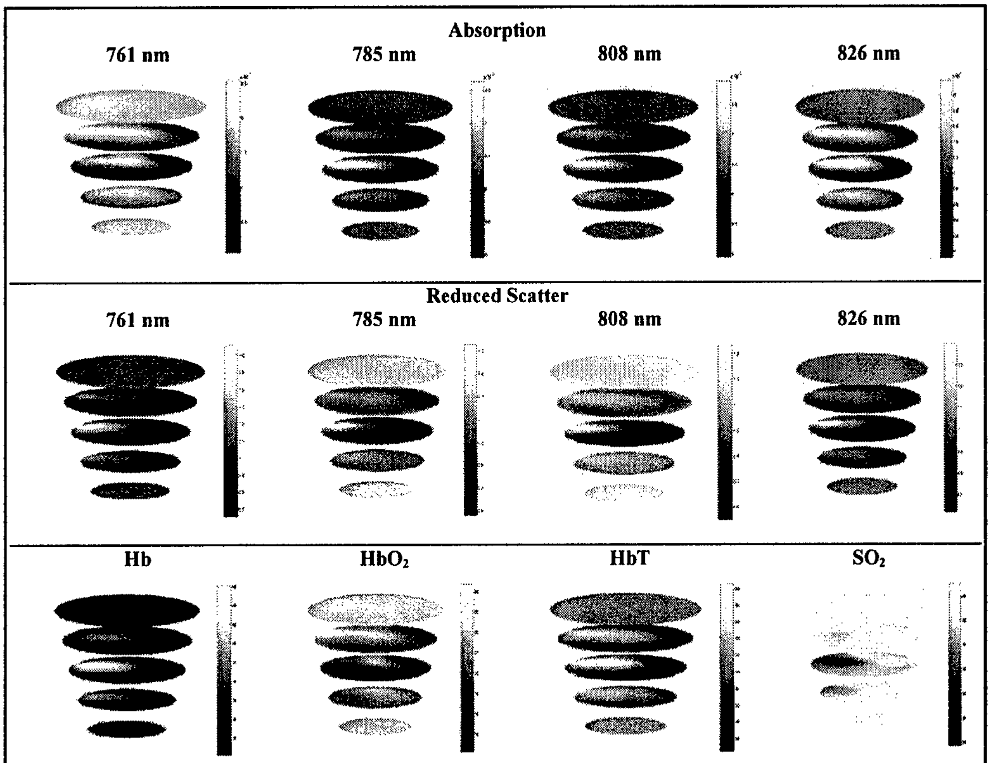

Figure 3. Reconstructed images of absorption (top row) and reduced scattering (middle row) at each wavelength from measured volunteer data, (volunteer A), as well as calculated maps of blood content; each slice represents a plane through the mesh, from the bottom near the nipple to the top near the chest. The images are coronal views of the cross section through the breast at the tenth iteration at the wavelengths.

The first case, (patient A), presented for standard screening mammography, which revealed a subtle nodular density and associated architectural distortion in the lateral aspect of the right breast. Pathology showed an invasive carcinoma of 20 mm size. 3D images of internal absorption and reduced scattering were recovered simultaneously from NIR data collected at each wavelength. The mesh used for the calculation of the Jacobian contained 8334 nodes corresponding to 41623 linear tetrahedral elements. For reconstruction basis, a second mesh of the same geometry was used, but with 2521 nodes, corresponding to 11575 linear tetrahedral elements. Images were reconstructed at four wavelengths of 761, 785, 808 and 826 nm, and they are shown in Figure 3. For image reconstruction the regularization parameter (λ) used was initially set to 10, and was allowed to decrease by a factor of $10^{1/4}$ if the projection error had decreased with respect to previous iteration. Images shown are those at the 10th iteration. Here the images are true 3D reconstructions and coronal slices at z = -60, -45, -30, -15 and 0 mm are shown. From the reconstructed images it can be seen that an anomaly is found within the mid-plane at approximately 9 o'clock position. The anomaly presents as an absorption variation with wavelength, whereas the reduced scatter is almost constant over all reconstructed wavelengths. The absorption images were used together with values of extinction coefficients for oxy and deoxy hemoglobin (HbO_2 and Hb respectively) for the calculation of Hb, HbO_2, total hemoglobin (HbT) and oxygen saturation (SO_2). The calculated 3D maps of Hb, HbO_2, total HbT and SO_2 are also shown in Figure 3.

Table 1. Values of Hemoglobin and oxygen saturation maps shown in Figures 15 and 16. The arrows show the increase(↑) or decrease (↓) of values within the region of interest with respect to the background.

	Hb (μM)	HbO_2 (μM)	HbT (μM)	SO_2 (%)	Tumor Type
Volunteer A (anomaly)	47.7 ↑	24.73 ↑	65.28 ↑	25.9 ↓	Invasive ductal carcinoma
Volunteer A (background)	32.87	20.23	53.11	38.11	
Volunteer B (anomaly)	10.76 ↑	15.56 ↑	22.56 ↑	69.26 ↑	Benign ductal hyperplasia
Volunteer B (background)	7.71	8.40	16.11	51.52	

From the calculated values of Hb it is seen that the anomaly shows a peak value of 47.7 μMole, compared to a background of 32.87 μM, whereas the HbO_2 image shows a peak value of 24.73 μM at a location on the periphery of the skin. The total hemoglobin value shows a peak at the location of the anomaly, with a value of 65.28 μM. SO_2 values, calculated by taking the ratio of oxygenated blood and total blood content, indicate a marked decrease at the location of the anomaly, with a value of 25.9%, as compared to a background value of 38.11%. These data are summarized in Table 1.

Volunteer B presented for standard screening mammography, which after biopsy revealed a benign ductal hyperplasia region within the right breast. From the reconstructed NIR images shown in Figure 4 an anomaly is found within the mid-plane, off-center near the nine o'clock position. Here, the anomaly indicates the variation of absorption with wavelength, with a peak value of 0.0055 mm^{-1} at 761 nm, and the reduced scattering images show a peak value of 3.3 mm^{-1}, also at 761 nm. The calculated maps of Hb shows a value of 10.76 μMs at the location of the anomaly, compared with a background of mean value of 7.7 μMs. The HbO_2 image shows a max value of 15.56 μMs, compared with a mean background value of 8.4 μMs. From the SO_2 images, the anomaly shows a marked increase to 69.26% in saturation, compared with a mean background saturation of 51.52% (Table 1).

For volunteer A, who had an invasive ductal carcinoma within the breast, the absorption and scattering increased within the region of interest. The calculated values of absorption were used together with extinction coefficients of Hb, HbO_2 to calculate deoxy, oxy and total hemoglobin maps, and from these data oxygen saturation images were generated. While the total hemoglobin level within the region of interest shows an increase with respect to background, the oxygen saturation shows a marked decrease within the same region. This trend is perhaps expected for malignant tissue, as one would expect a rise in blood content, due to an increase in blood vessel density, but since malignant tumors are more active, this would lead to a decrease in oxygen saturation.

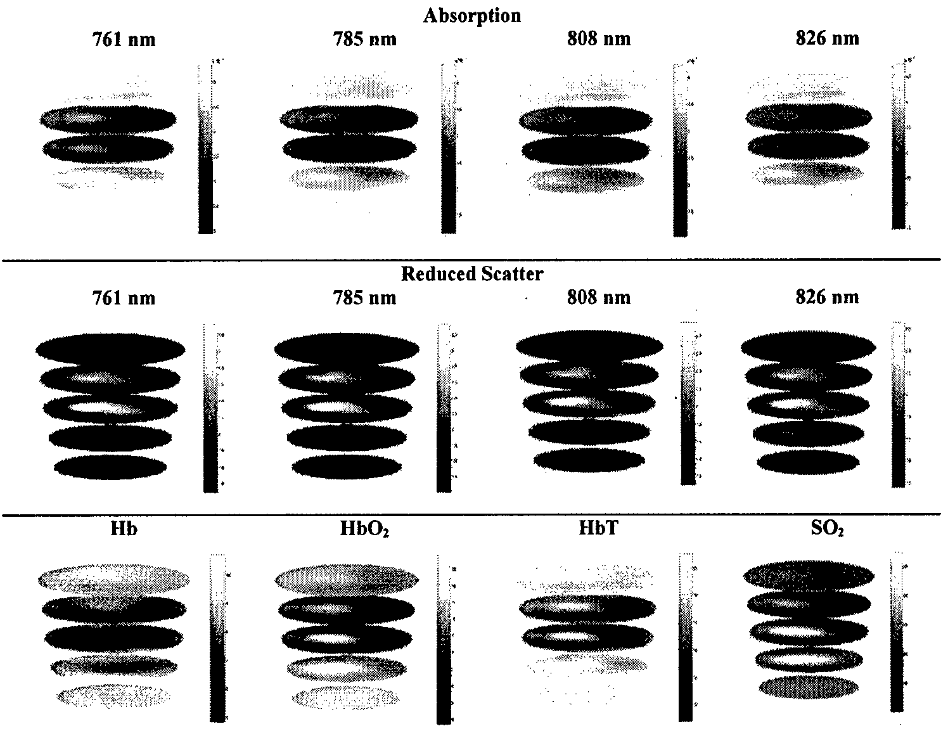

Figure 4 Reconstructed images of absorption (top row) and reduced scattering (middle row) at each wavelength from measured volunteer data, (volunteer B), as well as calculated maps of blood content; each slice represents a plane through the mesh, from the bottom near the nipple to the top near the chest. The images are coronal views of the cross section through the breast at the tenth iteration at the wavelengths.

For volunteer B, who had a benign ductal hyperplasia within the breast, the absorption and scattering also increased within the region of interest. For a benign condition, one might expect a rise in blood content due to an increase in blood vessel density, however benign tumors are not particularly more active, suggesting this would result in an increase in oxygen saturation as indicated.

It should be stressed that these results are preliminary, and further investigation is needed before one can claim tumor classification from tissue oxygenation maps. Further work is in progress with respect to building a larger database of such images, thereby allowing a proper and definite statistical analysis of the results.

Spectral imaging

Near Infra-Red (NIR) tomography is known for its ability to distinguish between malignant and normal tissue based on high-contrast arising from intrinsic processes such as angiogenesis and hypoxia in tumors. Absorption-based parameters can be recovered such as total hemoglobin, oxygen saturation and water fraction as well as scattering. These provide measures of physiology or pathophysiology related to the intra-vascular and extra-vascular spaces as well as composition of the tissue. Typically spectral tomography approaches must make use of only sparse data at discrete wavelengths instead of a complete spectrum, resulting in an insufficient measurement set for a unique solution. The reconstruction process is an ill-posed problem, which further amplifies this error leading to image artifacts and inaccuracy in quantifying the physiological parameters of the tissue. The current method illustrated here reduces the noise in recovery of chromophores, especially significant in water and scattering, by eliminating the need to reconstruct the absorption and scattering coefficients as intermediate endpoints. Instead, the chromophore concentrations and scatter parameters are reconstructed directly by incorporating the known linear spectral fit and scattering relationship with wavelength as constraints.

The method uses finite elements to model the diffusion equation and reconstructs images of five parameters: oxyhemoglobin (HbO), hemoglobin (Hb), water (H2O), scatter amplitude (a) and scatter power (b), with no assumptions on scatter amplitude (a) or scatter power (b). The results of the application of spectral constraints, in addition to showing a reduction in noise in the recovered chromophore concentrations, also provide evidence of reduced sensitivity to noise in measurements themselves.

The direct spectral reconstruction method has been tested using simulation and phantoms studies. As an illustration here, it has been applied to clinical tomography data obtained from measurements on a 66 year old subject with a 5-10 mm spiculated mass from mammography, later diagnosed as Invasive Ductal Carcinoma. The subject underwent the NIR exam in accordance with the Dartmouth protocol, and written consent was obtained from the subject. The position of the anomaly was provided by mammography and found to be at 11:30 o'clock in the cranocaudal view. The tumor was known to be located about 1cm from surface; data was collected in three planes. Reconstructed images are shown in Figure 5, for the plane in line with the tumor. The localized increase in Hb_T was observable and the contrast available was 1.7:1.0 in tumor versus background. The S_tO_2 image showed a decrease at the location of the tumor, with a contrast of 0.7:1. The corresponding S_tO_2 image with the conventional technique (not shown here) was noisier, and a similar decrease was not observed. The water image showed heterogeneity in the range 25 to 50%, which is considerably smaller than the range of 0 to 100% observed with the old method. Tighter data ranges are similarly observed in the scatter images, and artifacts in the separate wavelength technique have been completely suppressed in the spectral approach.

In summary, the new direct spectral reconstruction technique has been applied to homogeneous and heterogeneous data and the results have consistently shown reduced artifacts as well as improved quantitative accuracy in recovered parameters. With this new technique, higher hemoglobin content at site of tumor is observed in the clinical case, as well as lower oxygen saturation. The water and scattering images most significantly show improvement in all cases by reduction in the errors due to decreased artifacts.

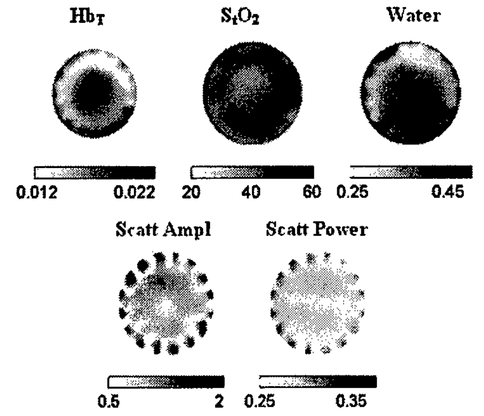

Figure 5. Hb_T [mM], S_tO_2 [%], water [%], 'a' and 'b' images are shown from measurements on a cancer subject with a 5-10 mm Invasive Ductal Carcinoma at the 11:30 o-clock position.

Incorporation of anatomical data

An important advance has been the culmination of several years of effort towards refining an MRI compatible NIR tomography system which works comfortably with a breast imaging coil to sample light signals transmitted through breast tissue. The system is shown in the figure 6(a) below, with the ring of 16 bifurcated fibers appearing in the positioning array Figure 2(b), with brass loaded springs, which gently push the fibers against the breast. A series of tissue simulating phantoms were created with gelatin, and a three-layer phantom is shown in the figure below, where an interior layer is included to mimic glandular-tissue surrounded by adipose tissue. A spherical interior object is also included to mimic a large tumor. These images have been used in a series of basic studies, where we are determining the optimal way to integrate spatial a priori information into the NIR tomography reconstruction.

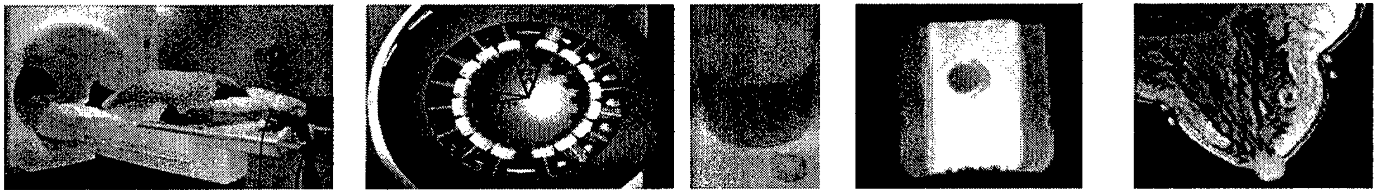
(a) (b) (c) (d) (e)

Figure 6. Image of the patient on the breast coil lying on the MRI bed is shown in (a). An image of the breast interface is shown in (b) with spring-loaded optical fibers arranged in a circle. A gelatin phantom is shown in (c) with varying concentrations of scatterer, absorber and copper sulphate solution, allowing simultaneous MRI and NIR phantom testing. MRI images of the phantom (d) and a breast (e) are shown where the presence of the array can be seen as indents in the phantom image, and as exterior fiducials in the breast image. On each fiber, a sponge ring fiducial is placed, allowing accurate imaging of the fiber tip on the breast tissue.

Images of the phantoms used in this system are shown in Figure 7, with segmentation of the three layers in the phantom. Without using the MRI interior structural information, the image reconstruction of this phantom would appear as shown in Figure 7(b). From the phantom data we note that it is possible to significantly improve the fitting of optical properties using a priori information. This latter approach is more accurate in estimating the peak value. Interestingly, if the regions were recovered as bulk values, reducing the number of estimators to only three, this approach leads to incorrect properties for the middle region. Thus, we have tentatively concluded that a priori information is better applied into the regularization parameter, than through segmentation and parameter reduction. Detailed analysis of the tradeoffs between parameter reduction (regionizing areas to be represented by a single pair of μ_a and μ_s' values) versus full reconstruction with regionization of the regularization parameter has been completed on phantom data sets. The conclusions to date indicate that regularization-based constraints are much more stable in the presence of noise, and that the covariance between nodes in the same medium is a key factor to include in this recovery. Thus, our working plan is to utilize interior information as carefully chosen variations in the regularization parameter.

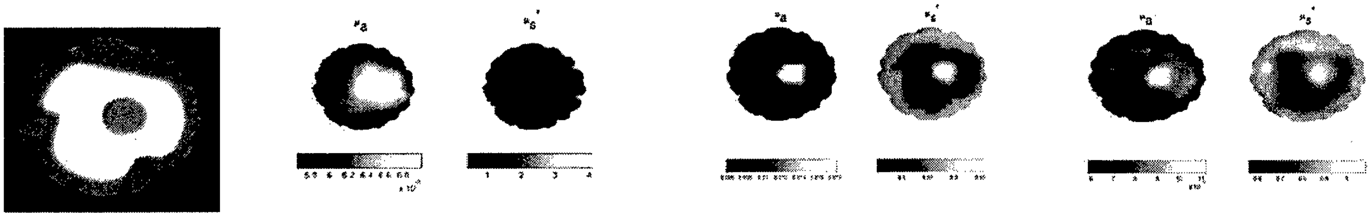

(a) (b) (c) (d)

Figure 7. Cross sectional MRI (a) and NIR (b and c) images of the tissue simulating phantom are shown, with the MRI image in (a) being used to define the exterior and interior boundaries between regions. In (b) our standard NIR image reconstruction results are shown, where the peak absorption coefficient is found to reach only 0.007 mm^{-1}, where the true value was 0.02 mm^{-1}. If the phantom interior regions obtained from the MR image are used to vary the regularization parameter, the peak value increased to 0.011 mm^{-1} (c), however if covariance between nodes is also incorporated (d), the value peaks (0.018 mm^{-1}) nearer the true level.

In Figure 8, images of a fatty/scattered breast are shown in (a) and a heterogeneously dense breast in (b), where in the latter breast, it is possible to segment the two major tissue types. These tissues are adipose on the exterior and fibro-glandular structure on the interior. Without using these segmented regions, the typical NIR image of this breast would be as shown in (c), whereas with the segmentation of the regions, the two tissue types can be fit to average bulk values, which agree with the expected numbers for these tissues (see figure caption).

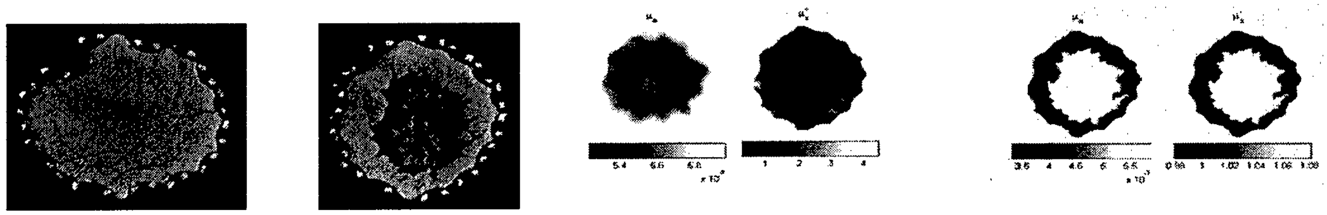

(a) (b) (c) (d)

Figure 8. Coronal MRI images of a fatty/scattered breast are shown in (a), and a heterogeneously dense breast in (b) in the breast imaging array, with the fiber fiducial markers demarking the fiber locations. The reconstructed NIR images of the breast shown in (b) are presented in (c) without a priori interior information and (d) with interior spatial information applied. The values of the absorption coefficient for the breast tissue types in the fatty and glandular regions are 0.0035 mm^{-1} and 0.006 mm^{-1}.

Conclusions

The project is continuing to reconstruct NIR images of clinical data to build the database of 3D images. Steps have also been taken as part of this project to achieve other aims specified by this project. A new and novel image reconstruction algorithm has been developed and implemented which allows the direct reconstruction of chromophore concentration and scattering functions of breast tissue. This not only allows a computationally efficient implementations, but also since all the data from all wavelength are used coupled together, a great reduction in image noise and artifact is seen. Finally, as a direct result of the 2nd aim, the project is beginning to develop, understand and implement a useful algorithm for the incorporation of a-priori information, not only in phantom studies, but also in clinical setups.

Publications List

S. Srinivasan, B. W. Pogue, S. Jiang, **H. Dehghani**, C. Kogel, S. Soho, J. J. Gibson, T. D. Tosteson, S. P. Poplack, K. D. Paulsen, "*Interpreting Hemoglobin and Water Concentration, Oxygen Saturation and Scattering Measured In Vivo by Near-Infrared Breast Tomography*" PNAS vol 100 no 21 pp 12349-12354 2003

X. Song, B. W. Pogue, s. Jiang, M. M. Doyley, **H. Dehghani**, T. D. Tosteson, K. D. Paulsen, "*Automated Region Detection Based Upon Contrast To Noise Ratio in Near-Infrared Tomography,*" Applied Optics 43(5) 1053-1062, 2004

H. Dehghani, M. M. Doyley, B. W. Pogue, S. Jiang, J. Geng and K. D. Paulsen, "*Breast deformation modeling for image reconstruction in near infrared optical tomography*" Phys. Med. Biol. Volume 49, Number 7, pp 1131-1146 2004.

S. Srinivasan, B. W. Pogue, **H. Dehghani**, S. Jiang, X. Song and K. D. Paulsen, "*Improved Quantification of Small Objects in Near-Infrared Diffuse Optical Tomography* Applied Optics Accepted 2004

B. W. Pogue, S. Jiang, **H. Dehghani**, C. Kogel, S. Soho, S. Srinivasan, X. Song, S. P. Poplack, and K. D. Paulsen, "*Characterization of Hemoglobin, Water and NIR Scattering in Breast Tissue: Analysis of inter-subject variability and menstrual cycle changes relative to lesions*" JBO, 9(3) 541-552, 2004.

Subhadra Srinivasan, Brian W. Pogue, **Hamid Dehghani**, Shudong Jiang, Xiaomei Song, Keith D. Paulsen, "*Effect of image reconstruction bias upon spectroscopy-based quantification of chromophores in nearinfrared tomography*" In Biomedical Topical Meetings on CD-ROM (The Optical Society of America, Washington, DC) 2004.

Ben A. Brooksby, Shudong Jiang, Gordon Ehret, **Hamid Dehghani**, Brian W. Pogue, Keith D. Paulsen, "*Development of a system for simultaneous MRI and Near-infrared diffuse tomography to diagnose breast cancer* In Biomedical Topical Meetings on CD-ROM (The Optical Society of America, Washington, DC) 2004.

Heng Xu, **Hamid Dehghani**, Brian W. Pogue, Keith D. Paulsen, Roger Springett, Jeff F. Dunn, "*Optical tomography system based on second-differential spectroscopy for small animal brain study* In Biomedical Topical Meetings on CD-ROM (The Optical Society of America, Washington, DC) 2004.

Brian Pogue, Shudong Jiang, Subhadra Srinivasan, Xiaomei Song, **Hamid Dehghani**, Keith Paulsen, Tor Tosteson, Christine Kogel, Sandra Soho, Steven P. Poplack, "*Near-infrared scattering spectrum differences between benign and malignant breast tumors measured in vivo with diffuse tomography* In Biomedical Topical Meetings on CD-ROM (The Optical Society of America, Washington, DC) 2004.

Hamid Dehghani, Brian W. Pogue, Marvin M. Doyley, Jason Geng, Keith D. Paulsen, "*Breast deformation in near infrared optical tomography* In Biomedical Topical Meetings on CD-ROM (The Optical Society of America, Washington, DC) 2004

Appendices

Four papers are included as appendices, which are as a direct result of the project funding:

1. **H. Dehghani**, M. M. Doyley, B. W. Pogue, S. Jiang, J. Geng and K. D. Paulsen, "*Breast deformation modeling for image reconstruction in near infrared optical tomography*" Phys. Med. Biol. Volume 49, Number 7, pp 1131-1146 2004.
2. **Hamid Dehghani**, Brian W. Pogue, Marvin M. Doyley, Jason Geng, Keith D. Paulsen, "*Breast deformation in near infrared optical tomography* In Biomedical Topical Meetings on CD-ROM (The Optical Society of America, Washington, DC) 2004
3. Subhadra Srinivasan, Brian W. Pogue, Shudong Jiang, **Hamid Dehghani**, Keith D. Paulsen, "*Spectrally-Constrained Chromophore and Scattering Reconstruction for In Vivo NIR Tomography*" Optics letters, Submitted 2004
4. Ben Brooksby, Shudong Jiang, Christine Kogel, Marvin Doyley, **Hamid Dehghani**, John B. Weaver, Steven P. Poplack, Brian W. Pogue, and Keith D. Paulsen, "*Magnetic Resonance-Guided Near-Infrared Tomography of the Breast*", Review of Scientific Instruments, Submitted 2004

APPENDIX 1

INSTITUTE OF PHYSICS PUBLISHING PHYSICS IN MEDICINE AND BIOLOGY

Phys. Med. Biol. 49 (2004) 1131–1145 PII: S0031-9155(04)74363-8

Breast deformation modelling for image reconstruction in near infrared optical tomography

Hamid Dehghani[1], **Marvin M Doyley**[2], **Brian W Pogue**[1], **Shudong Jiang**[1], **Jason Geng**[3] **and Keith D Paulsen**[1]

[1] Thayer School of Engineering, Dartmouth College, Hanover, NH 03755, USA
[2] Department of Radiology, Dartmouth Medical School, Hanover, NH 03755, USA
[3] Genex Technologies Inc., 10605 Concord Street, Suite 500 Kensington, MD 20895-2504, USA

Received 8 October 2003
Published 18 March 2004
Online at stacks.iop.org/PMB/49/1131 (DOI: 10.1088/0031-9155/49/7/004)

Abstract

Near infrared tomography (NIR) is a novel imaging technique that can be used to reconstruct tissue optical properties from measurements of light propagation through tissue. More specifically NIR measurements over a range of wavelengths can be used to obtain internal images of physiologic parameters and these images can be used to detect and characterize breast tumour. To obtain good NIR measurements, it is essential to have good contact between the optical fibres and the breast which in-turn results in the deformation of the breast due to the soft plasticity of the tissue. In this work, a tissue deformation model of the female breast is presented that will account for the altered shape of the breast during clinical NIR measurements. Using a deformed model of a breast, simulated NIR data were generated and used to reconstruct images of tissue absorption and reduced scatter using several assumptions about the imaging domain. Using either a circular or irregular 2D geometry for image reconstruction produces good localization of the absorbing anomaly, but it leads to degradation of the image quality. By modifying the assumptions about the imaging domain to a 3D conical model, with the correct diameter at the plane of NIR measurement, significantly improves the quality of reconstructed images and helps reduce image artefacts. Finally, assuming a non-deformed breast shape for image reconstruction is shown to lead to poor quality images since the geometry of the breast is greatly altered, whereas using the correct deformed geometry produces the best images.

(Some figures in this article are in colour only in the electronic version)

1. Introduction

Near infrared (NIR) tomography is an emerging alternative imaging method used to image physiologic parameters of biological tissue *in vivo* such as water and haemoglobin.

0031-9155/04/071131+15$30.00 © 2004 IOP Publishing Ltd Printed in the UK

Measurements of light propagation (600–900 nm) within tissue can be used to map internal chromophore concentrations within tissue. Light is transmitted through tissue using multiple input and output locations on the surface of the region to be imaged, similar to a fan-beam x-ray computed tomography geometry, but using optical fibres for delivery and pick up of the light signals. The intensity and path-length distributions of the exiting photons provide information about the optical properties of the transilluminated tissue using a model-based interpretation where photon propagation is simulated by diffusion theory. Using these techniques implemented in hardware and software, NIR optical tomography becomes an inherently three-dimensional imaging method and is used to reconstruct physiologically relevant chromophore distributions from the region under investigation (Eda *et al* 1999, Fantini *et al* 1999, Boas *et al* 2001, Hebden *et al* 2001, Pogue *et al* 2001, McBride *et al* 2002, Dehghani *et al* 2003a, 2003b, 2003c). The main interest in this study lies in the ability to detect and characterize tumours within the female breast (Pogue *et al* 2001, Brooksby *et al* 2003). Since the absorption and scattering of light in tissue is a function of its optical properties, and hence its physiological state, the aim is to obtain images of internal optical absorption coefficient μ_a, reduced scattering coefficient μ_s' and ultimately images of total haemoglobin and oxygen saturation distributions. These images should in principle provide information about the physiological state of the tissue under investigation and help identify and characterize tumours within the breast. However, in recent years it has become apparent that the external shape of the tissue can dramatically impact the quality of the reconstruction, and this is largely due to mismatch between the model prediction and the actual shape of the tissue boundary. In this study, a focused effort has been put forward to examine the extent to which external boundary changes will degrade image quality and, more importantly, how this could be corrected with appropriate model-based analysis.

To obtain clinical measurements with a sufficient signal-to-noise ratio, it is key to ensure that good contact exists between the optical fibres and the tissue. More specifically to our studies, the patient lies prone on the measurement bed, which contains a single opening for the breast. The breast is suspended freely through this opening, below which the optical fibres are brought into contact with the breast. Normally, the optical fibre arrangement consists of a total of 48 fibres, 16 fibres in three separate planes. However, for the purpose of this work only one plane of 16 fibres is considered. The fibres need to make full contact with the breast for a good and adequate NIR measurement.

The breast is a soft tissue, which will deform and alter its shape on the application of external pressure. The amount of deformation is a function of the tissue mechanical properties and the amount of displacement and the external pressure applied by the optical fibre array. In most image reconstruction algorithms, the general assumption is made that the region under investigation is a uniform circular (2D) or conical or cylindrical (3D) domain. Little work has been done to evaluate the effect of any incorrect geometry in image reconstruction. For simple symmetric geometries, for example a 3D cylinder, work has been described to accurately calibrate the data to account for 2D/3D mismatch (Hillman *et al* 2000). More recently, work has been done with regard to neonatal head imaging that a slight change to the geometry model, both in terms of geometry and mesh, will result into large change in modelled data (Gibson *et al* 2003a).

In this work, the effect of such assumptions is investigated by creating a deformation of the breast model in 3D to generate simulated clinical data. Images are then reconstructed using various assumptions regarding the imaging domain including a circular or irregular 2D models as well as a 3D conical shaped model and the non-deformed breast model to evaluate image quality. An important part of this modelling effort is the recent advances which have been made in modelling soft tissue deformation (Paulsen *et al* 1999, Doyley *et al* 2000, Van Houten *et al*

2000). Beyond this, it is also becoming established that soft tissue elastic properties can be directly measured with elastography imaging *in vivo*, thereby providing the key information needed for predicting the deformation of tissue under force or displacement conditions. In this study, this displacement modelling was used along with the NIR tomography modelling to create a comprehensive three-dimensional prediction of how to approach appropriate modelling of deformed tissue that is being imaged with NIR tomography.

2. Theory

2.1. Breast deformation model

Soft tissues exhibit nonlinear elastic behaviour (Fung 1993). Nevertheless, it can be considered a linear elastic material in situations where the deforming forces produce infinitesimal deformations (i.e. $\leqslant 5\%$) (Timoshenko and Goodier 1970). For the purpose of this study, the breast was modelled as linear isotropic pseudo-incompressible (i.e. Poisson's ratio $(\nu) = 0.495$ (Fung 1993)). Under these assumptions and ignoring internal body force, the governing elasticity equations for quasi-static deformation are given by Timoshenko and Goodier (1970) and Fung (1993)

$$(\lambda + \mu)\nabla(\nabla \cdot u) + \mu\nabla^2 u = 0 \tag{1}$$

for internal nodes in domain Ω, and

$$((\lambda + \mu)\nabla(\nabla \cdot u) + \mu\nabla^2 u) \cdot \hat{n} = h \tag{2}$$

for nodes on the boundary $\delta\Omega$.

Here $\hat{n}$ represents a unit vector directed outwards from Ω, and h represents the traction on the surface or boundary of the breast. Note that u represents the displacement components in all coordinate directions, and μ and γ are Lame's elastic constants. For an isotropic medium these constants are related to the more familiar Young's modulus (E) and the Poisson's ratio (ν) by

$$\mu = \frac{E}{2(1+\nu)} \qquad \lambda = \frac{\nu E}{(1+\nu)(1-2\nu)}. \tag{3}$$

The first Lame's elastic constant (i.e. μ) is generally known as shear modulus.

It should be stated that in this study, the breast was assumed to be traction free (i.e. no other forces are associated) and internal body forces were neglected, thus the problem is solved by imposing a prescribed displacement (i.e. induced when the optical fibres are coupled to the breast) as described in Doyley *et al* (1999).

2.2. Light propagation model

Under the assumption that scattering dominates absorption for NIR light in tissue, the Boltzmann transport equation can be simplified to the diffusion approximation, which in the frequency domain is given by

$$-\nabla \cdot D\nabla\Phi(r,\omega) + \left(\mu_a + \frac{\mathrm{i}\omega}{c}\right)\Phi(r,\omega) = q_0(r,\omega) \tag{4}$$

where $q_0(r,\omega)$ is an isotropic source, $\Phi(r,\omega)$ is the photon fluence rate at position r and $D = \frac{1}{3(\mu_a+\mu_s')}$ is the diffusion coefficient. We use the Robin (Type III) boundary condition:

$$\Phi(\gamma) + \frac{D}{\alpha}\hat{n} \cdot \nabla\Phi(\gamma) = 0 \tag{5}$$

where α is a term which incorporates reflection as a result of refractive index mismatch (Schweiger *et al* 1995, Dehghani *et al* 2003c) at the boundary, and $\hat{n}$ is the outward pointing normal to the boundary ($\delta\Omega$) at γ.

We assume that the data are represented by a nonlinear operator $y^* = F[\mu_a, D]$, where our data y^* are a complex vector having a real and imaginary components, which are mapped to log amplitude and phase shift in measurement. Then the image reconstruction method is posed as a solution to the following expression:

$$(\hat{\mu}_a, \hat{D}) = \arg\min_{\mu_a,\kappa} \|(y^* - F(\mu_a, D))\| \tag{6}$$

where $\|\cdot\|$ is the weighted L2-norm, representing the square root of the sum of the squared elements, $\hat{\mu}_a$ is a vector of the absorption coefficients and $\hat{D}$ is a vector of the diffusion coefficients. The magnitude of this is sometimes referred to as the projection error and provides a value for determining the convergence of the iterative reconstruction algorithm.

In this study, a finite-element method (FEM) is used as a general and flexible method for solving the forward problem in arbitrary geometries (Arridge *et al* 1993, Jiang *et al* 1996). In the inverse problem, where the goal is to recover internal optical property distributions from boundary measurements, it is assumed that $\mu_a(\mathbf{r})$ and $D(\mathbf{r})$ are expressed in a basis with a limited number of dimensions (less than the dimension of the finite element system matrices). A number of different strategies for defining reconstruction bases are possible; in this paper a linear pixel basis (Schweiger and Arridge 1999) is used. To find $(\hat{\mu}_a, \hat{D})$ in equation (6) we have used a Levenberg–Marquardt algorithm, where we repeatedly solve:

$$\hat{a} = J^T(JJ^T + \rho I)^{-1}\hat{b} \tag{7}$$

where $\hat{b}$ is the data vector, $\hat{b} = [y^* - F[\mu_a, D]]^T$, $\hat{a}$ is the solution update vector, $\hat{a} = [\delta\hat{D}; \delta\hat{\mu}_a]$. Here, ρ is the regularization factor and J is the Jacobian matrix for our model which is calculated using the Adjoint method (Arridge and Schweiger 1995, Dehghani *et al* 2003b, 2003c).

3. Methods

3.1. Breast deformation

A volume mesh of a female breast of a volunteer was created from surface image data that was acquired using a 3D surface camera (Rainbow 3D Camera, Genex Technologies, Kensington MD). The 3D camera projects structural illumination patterns onto the object and calculates 3D surface profile described by over 300 000 data points (Geng 1996, Galdino *et al* 2002). A volume mesh is then generated using the Delaunay algorithm. The mesh has a geometry of 130 × 136 × 60 mm, figure 1(a), and contained 15 501 nodes corresponding to 61 171 linear tetrahedral elements. The diameter of the breast at its mid-plane where optical fibre array will be applied is approximately 88 mm. To calculate the deformation due to 16 equally spaced optical fibres being applied at the mid-plane of the breast, i.e. $z = -30$ mm, it is assumed that each optical fibre pushed the breast so that the final breast diameter at $z = -30$ mm is 70 mm, and that the diameter of each optical fibre is 6 mm. The modelled elastic properties of tissue, equation (3), were assumed as isotropic and homogenous with Young's modulus of 20 kPa (Krouskop *et al* 1998) and Poisson's ratio of 0.495 (Fung 1993). Further, it was assumed that the topmost part of the mesh, i.e. $z = 0$ mm was not allowed to move since it is connected to the chest. Using this applied displacement as a boundary condition, the displacement at all nodes due to the application of the optical fibres was calculated and a deformed mesh was created, figure 1(b).

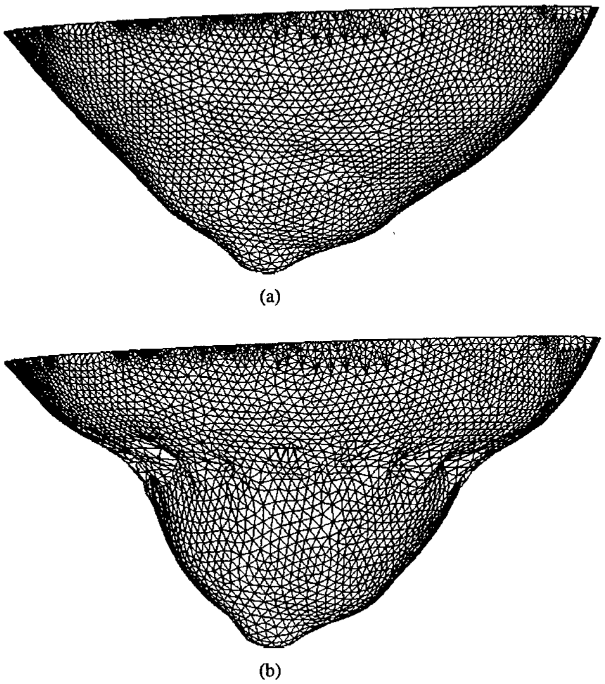

(a)

(b)

Figure 1. Volume mesh of the (a) normal suspended breast and (b) the deformed mesh after the application of the optical fibre array.

3.2. Simulation of data from deformed breast

In order to accurately simulate the clinical settings, two localized anomaly regions were placed within the mid-plane of the normal breast, both at $z = -30$ mm, figure 2(a). First was an absorbing anomaly, 19 mm from the surface and a radius 10 mm with a coefficient value of 0.03 mm^{-1}. Second was a reduced scattering anomaly, also 19 mm from the surface but with a radius of 7.5 mm and a value of 3 mm^{-1}. These anomalies were chosen as they represent the size and contrast we aim to image and so that absorption and scatter separation can also be investigated. The background optical properties were modelled with an absorption coefficient of 0.01 mm^{-1} and a reduced scatter coefficient of 1.0 mm^{-1}. For the deformed breast model the same optical properties of the normal breast were assumed (the anomalies were also assumed to have the same elastic properties of the background). Once the deformation of the model was calculated, it was assumed that the anomalies were free to move, depending on the elastic properties of the breast, figure 2(b). It is interesting to note that the displacement of the anomalies is not so much dependent on the mesh density of the breast, but more dependent on the mechanical properties, applied pressure and non-symmetric nature of the breast.

Using the deformed mesh, together with the displaced anomalies, data were simulated for 16 equally circularly spaced optical fibres placed at $z = -30$ mm. Amplitude and phase data were simulated at 100 MHz, and 1% noise was added. These data were then used as simulated patient data in the following sections. In addition, to allow data calibration as done using clinical data, and discussed elsewhere (Dehghani *et al* 2003c, McBride *et al* 2003), the data were simulated for 16 equally spaced optical fibres placed in a circle around the mid-plane of a

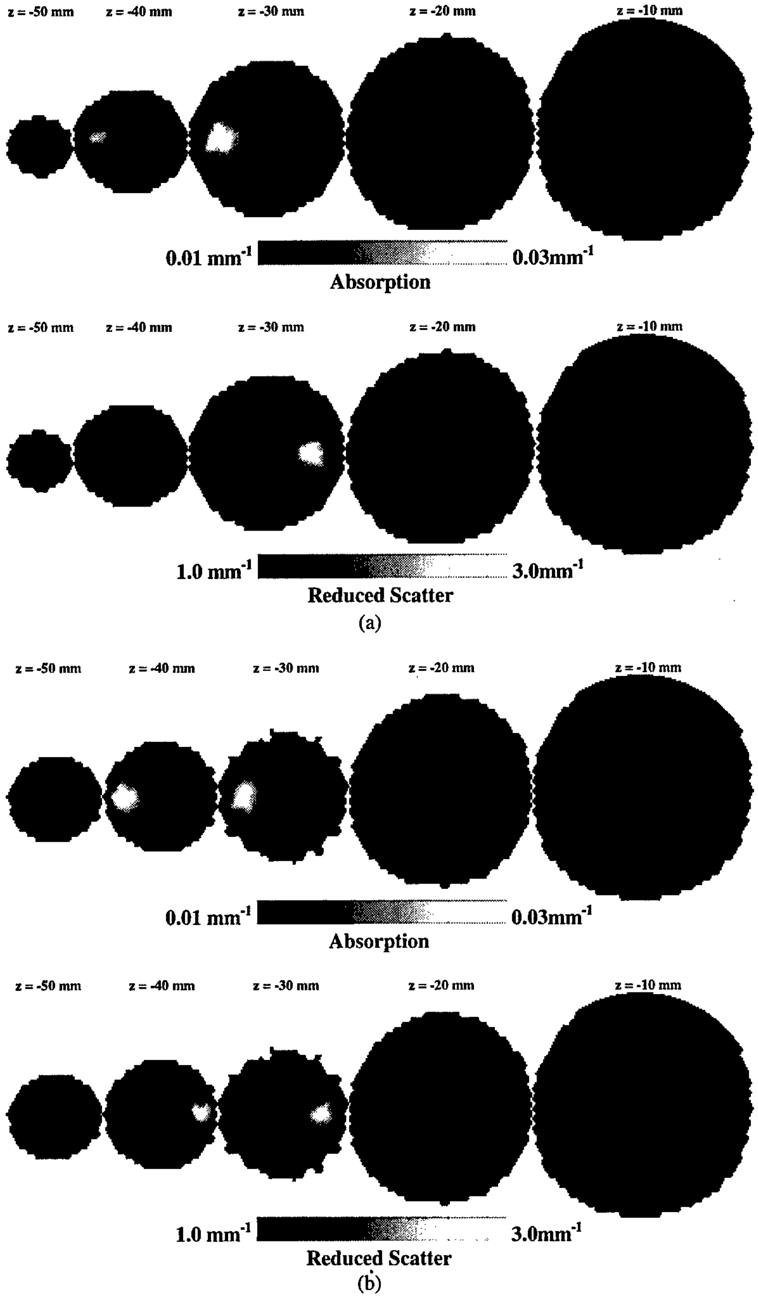
z = -50 mm
z = -40 mm
z = -30 mm
z = -20 mm
z = -10 mm
0.01 mm-1
0.03mm-1
Absorption
z = -50 mm
z = -40 mm
z = -30 mm
z = -20 mm
z = -10 mm
1.0 mm-1
3.0mm-1
Reduced Scatter
(a)
z = -50 mm
z = -40 mm
z = -30 mm
z = -20 mm
z = -10 mm
0.01 mm-1
0.03mm-1
Absorption
z = -50 mm
z = -40 mm
z = -30 mm
z = -20 mm
z = -10 mm
1.0 mm-1
3.0mm-1
Reduced Scatter
(b)

Figure 2. 2D coronal slices through (a) the normal breast mesh and (b) the deformed breast mesh, showing the position of the anomalies. The most right-hand slice is near the chest while the most left-hand slice is near the nipple.

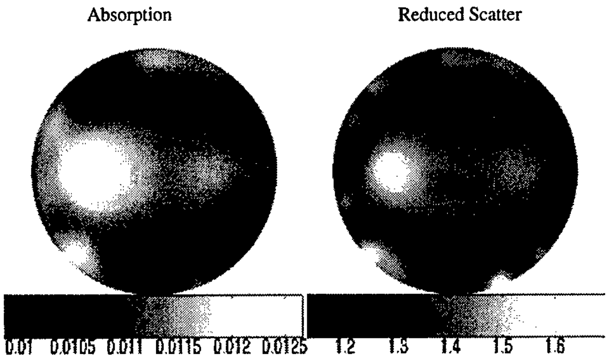

Figure 3. 2D simultaneous reconstruction of absorption and reduced scatter from deformed breast model simulated data. The mesh used for the reconstruction is a circular mesh whose diameter is the same as the optical fibre array diameter used to deform and simulate data NIR from the breast model.

non-deformable cylindrical model with a known homogenous background optical properties. The same calibration data file has been used for all presented reconstructions.

3.3. Image reconstruction using 2D meshes

Using the computed data for the deformed mesh and the reference phantom, as simulated measurements with 1% random noise added, the data were calibrated (Dehghani *et al* 2003c, McBride *et al* 2003) and images were reconstructed using two different 2D meshes. Assuming that the imaging domain was a circular domain with a radius equal to the radius of the optical fibre array, i.e. 35 mm, images were reconstructed and the results are shown in figure 3. The circular mesh used contained 1785 nodes corresponding to 3418 linear triangular elements. For the reconstruction basis (basis used for the update of the optical parameters), a 20 × 20 regular grid (piecewise linear) was used and the initial regularization parameter was set to 100. Images shown here, and all following sections are at iteration level where the projection error was within 5% of the previous iteration. In the 2D reconstruction cases, this projection error was reached typically in the 7th iteration.

It is evident from figure 1(b) that the breast at the plane of measurement, i.e. $z = -30$ mm, was no longer circular. In order to evaluate if a more correct *a priori* information regarding the 2D boundary at the plane of measurement would be useful, a 2D irregular mesh, with a boundary whose profile is the same as the boundary at $z = -30$ mm for the deformed mesh, was created and used for image reconstruction. The resulting images reconstructed on this mesh are shown in figure 4. The irregular mesh used contained 2405 nodes corresponding to 4619 linear triangular elements. For the reconstruction basis, a 20 × 20 regular grid was used and the initial regularization parameter was set to 100. Thus in this case, the irregular boundary was matched, but still the image reconstruction was approximated by a 2D forward solution.

3.4. Image reconstruction using 3D conical mesh

In the next section, we examined the improvement if a true 3D forward calculation was assumed, but with a regular geometry. In a previous work, it was hypothesized that given a set of 3D patient data, those images could be reconstructed with reasonable accuracy if

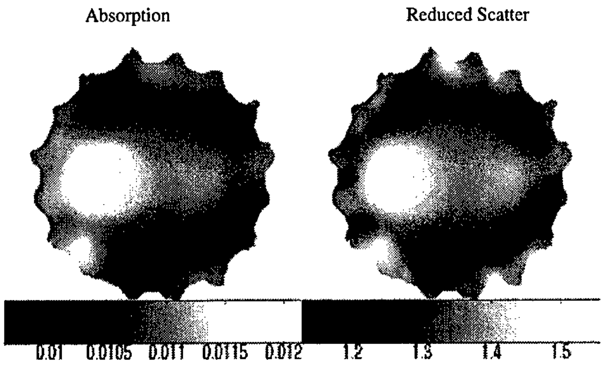

Figure 4. 2D simultaneous reconstruction of absorption and reduced scatter from deformed breast model simulated data. The mesh used for the reconstruction is an irregular whose boundary is the same as the boundary of the deformed breast mesh at $z = 30$ mm.

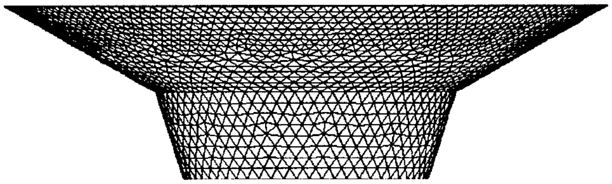

Figure 5. The conical shaped volume mesh. The geometry of the mesh is such that the diameter at the mid-plane corresponds to the diameter of the optical fibre array used to deform and simulate NIR data of the breast model. The diameter at 20 mm above and 20 mm below the NIR measurement plane of the deformed breast were also used to set the upper and lower bound of the cone model.

the breast was assumed to be a conical shaped model (Dehghani *et al* 2003c). To create a conical mesh, the information about the diameter of the measurement fibre array as well as the diameter of the breast at 20 mm above and 20 mm below the measurement plane was used, which would include all boundary information other than effects due to tissue bulging. Following this procedure, a conical shaped volume mesh was created, as shown in figure 5, which shows the upper chest wall and the confined partial-conical breast shape as a regular geometry approximation to the circularly compressed breast shape. The mesh contained 9332 nodes corresponding to 42 281 linear tetrahedral elements and was created using NETGEN (Schoberl). Using this mesh and the simulated data for the deformed breast mesh, images were reconstructed and the results are shown in figure 6.

For the reconstruction basis, a $20 \times 20 \times 10$ regular grid was used and the initial regularization parameter was set to 100. The images shown here and all through the following section are at iteration level where the projection error was within 5% of the previous iteration. These presented from the 3D cases are from the 14th iteration.

3.5. Image reconstruction using the normal and deformed breast mesh

Assuming that correct information regarding the breast is available, before the application of the optical fibre array, the normal, non-deformed mesh was used as shown in figure 1(a),

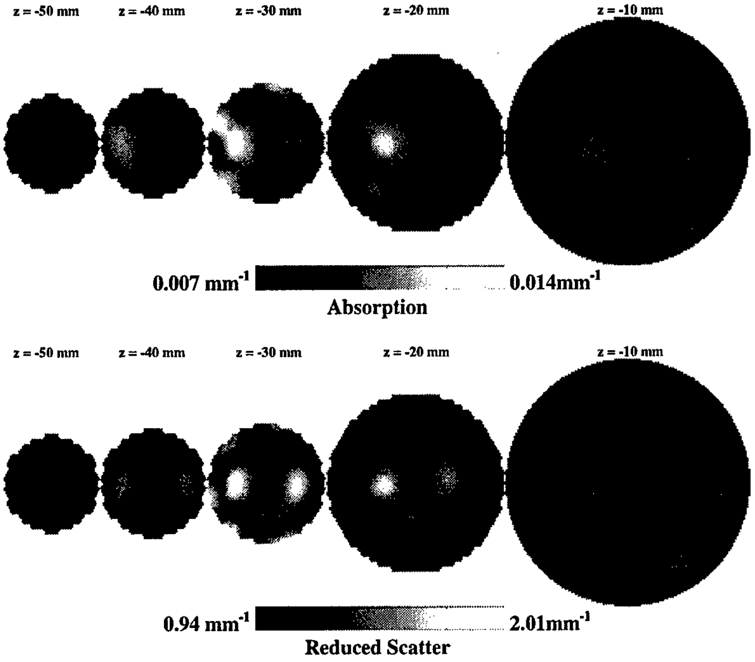

Figure 6. 3D simultaneous reconstruction of absorption and reduced scatter from deformed breast model simulated data. The mesh used for the reconstruction is the mesh shown in figure 5. The most right-hand slice is near the chest while the most left-hand slice is near the nipple.

as the reconstruction mesh for the images shown in figure 7. The reconstruction basis and parameters used were the same as for the conical model already described. Finally, to show the best possible reconstruction, the deformed mesh, figure 1(b) was used for reconstruction of images and these are shown in figure 8.

4. Results

The deformed breast mesh, as a result of applying a circular optical fibre array at $z = 30$ mm, is shown in figure 1(b). It is evident that the mesh has been compressed at the plane of applied displacement with slight bulging in-between each optical fibre. The breast mesh has also extended in the z direction near the nipple to maintain a constant volume as the nodes on the chest wall are assumed fixed. Although the mechanical properties of the tissue are assumed constant, it is interesting to note that the modelled anomalies have also been displaced due to the deformation, figures 2(a) and (b). Both the anomalies have been reduced in diameter, but have extended in the z direction as a result of the applied deformation.

Two-dimensional images reconstructed using the simulated deformed breast data are shown in figures 3 and 4. In both cases where a circular or an irregular boundary was used, good images were recovered in terms of localization of the absorption anomaly (within 1.2 mm for the circular model, and 2.0 mm for the irregular model). The recovery of the

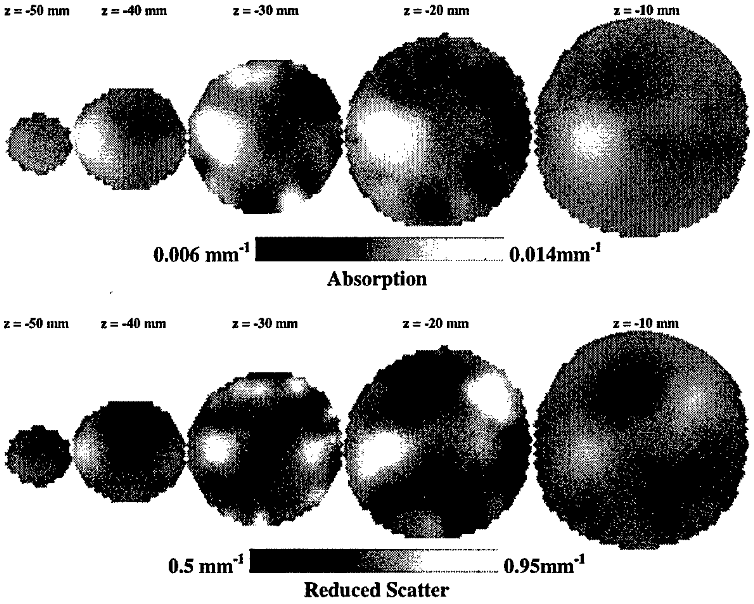

Figure 7. 3D simultaneous reconstruction of absorption and reduced scatter from deformed breast model simulated data. The mesh used for the reconstruction is the mesh shown in figure 1(a). The most right-hand slice is near the chest while the most left-hand slice is near the nipple.

reduced scattering anomaly was not as good as the absorption, and both sets of images contain large boundary artefacts. The background values of both the absorption and reduced scatter were close to the expected value, however, the target absorption value is less than 50% than expected.

Three-dimensional images reconstructed assuming a conical shaped breast are shown in figure 6. In that case, both the absorption and the scattering anomalies were recovered with good localization (within 2.00 mm for both the absorption and scattering objects) and with little boundary artefacts. Since the measured data were about the mid-plane of the breast, and the modelled cone geometry also had the optical fibres around its mid-plane, the objects recovered are centred at $z = -30$ mm. Here the background values of absorption and scatter were a little lower than expected values, however, the absorption anomaly had a maximum value of 0.014 mm^{-1} and the scattering object had a maximum value of 2 mm^{-1}.

Images reconstructed using the assumption of correct non-deformed breast geometry are shown in figure 7. In this case, although the absorbing anomaly has been reconstructed, the reduced scattering images contain large artefacts. The background absorption and scatter values are about 0.006 mm^{-1} and 0.5 mm^{-1}, respectively, while the maximum absorption for the anomaly is 0.014 mm^{-1}. Finally, images reconstructed assuming correct 3D deformed boundary are shown in figure 8. Here, both the absorbing and scattering regions have been recovered within less than 1.00 mm of expected location, giving great localization accuracy. There exists some cross talk between the absorbing and scattering anomalies. The background absorption and scatter values are about 0.01 mm^{-1} and 0.98 mm^{-1}, respectively, while the maximum absorption and scatter values for the anomaly is 0.013 mm^{-1} and 1.3 mm^{-1}, respectively.

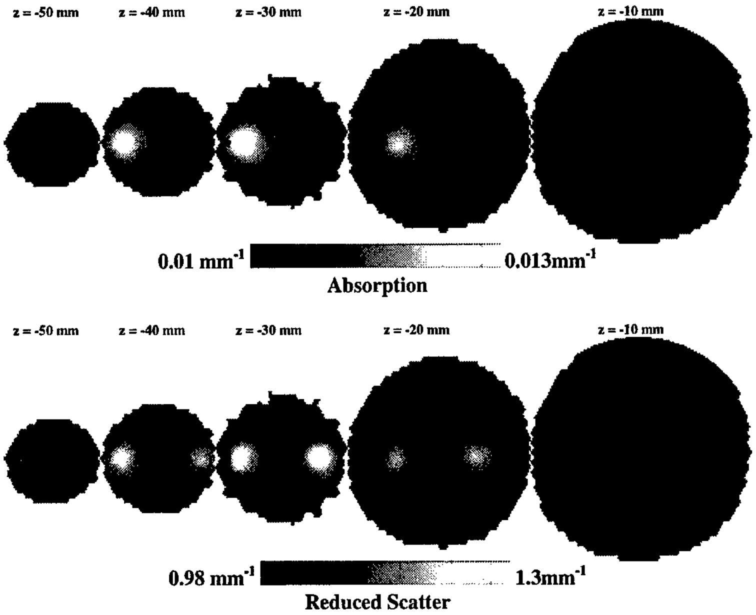

Figure 8. 3D simultaneous reconstruction of absorption and reduced scatter from deformed breast model simulated data. The mesh used for the reconstruction is the mesh shown in figure 1(b). The most right-hand slice is near the chest while the most left-hand slice is near the nipple.

5. Discussions

The deformation of the breast due to the application of 16 circular equally spaced optical fibres has been modelled using a computational mechanic model. Using this deformed model which also contains a single absorbing and a single scattering perturbations, data were simulated and 1% noise was added to more adequately represent clinical measurements. Using these simulated data, reconstructed images of absorption and reduced scatter were generated simultaneously using various different geometries of the mesh upon which the reconstruction would take place. In the first case, it was assumed that the model used for reconstruction was circular with a radius equal to the radius of the optical fibre array after breast compression, which was 35 mm. The reconstructed images have shown good accuracy in the localization of the absorbing object with a maximum absorption value of 0.014 mm^{-1}. The recovery of the scattering objects is much poorer than the absorbing anomaly, which can be attributed, perhaps, to its small size (15 mm diameter). There exist boundary artefacts in both the absorbing and scattering images. It is possible to improve the quality of the reconstructed 2D images by using several methods, including the use of various regularization parameters and/or use of *a priori* information. A good method to improve the reconstructed images in this case would be to segment the reconstructed images shown in figure 3, and use these as *a priori* information to more accurately obtain quantitative results. The application of such algorithm is discussed elsewhere, and has been found to provide superior results (Srinivasan *et al* 2004). In the case of knowing and using correct 2D boundary information in image reconstruction, figure 4, no useful improvement was seen. Although correct information was added to the reconstruction with regard to the boundary, the image reconstruction algorithm was still constrained to be 2D. While it has been shown many times that the 2D geometry can be used to recover accurate image data from NIR tomography with a circular boundary (Pogue and McBride 1999), it is not surprising, perhaps, to find that this simplification does not continue to work as the exterior boundary becomes more complex in shape. The reconstruction mesh is no longer symmetric and contains many irregular edges, which gives rise to high frequency noise at the boundary, and those changes occur symmetrically around each optical fibre making the calculation even more dependent upon the 3D geometry out of the plane of imaging.

Next for the case where the imaging domain was assumed to be conical in shape, the reconstructed images were shown in figure 6. Here it was assumed that the mid-plane of the cone had a radius equal to the radius of the optical fibre array after breast compression. Further, it was assumed that the measurements of the diameter of the breast 20 mm above and 20 mm below the measurement plane were known. Using these data, a conical shaped mesh could be created for any patient exam as shown in figure 5. The reconstructed images had recovered both the absorbing and scattering anomalies with reasonable success. The calculated background values for absorption and scatter were 0.007 mm^{-1} and 0.94 mm^{-1}, respectively. There exists a small cross talk between the absorption and reduced scatter images, plus artefacts at the boundary of the images. The qualitative and quantitative accuracy of the conical shaped model reconstruction are better than the 2D circular case, simply because a more accurate 3D model, rather than a 2D model is used.

In the case where it is assumed that the exact breast geometry was known, but have ignored information regarding the compression due to the optical fibres, the resulting images are shown in figure 7. Here, although the absorption anomaly was recovered with relatively good accuracy, the reduced scattering image contains a large artefact. Furthermore, the calculated background values for absorption and scatter are 0.006 mm^{-1} and 0.5 mm^{-1}, respectively, which are much lower than expected. These images are, perhaps, not as accurate and useful as the conical geometry case, since, although there is a more accurate 3D model, the diameter of the breast was not correct, particularly within the measurement plane, i.e. $z = -30$ mm. Finally, for the case of using a geometrically correct deformed mesh to reconstruct, the images are shown in figure 8. Here, the reconstructed images of absorption and scatter were found with superior localization accuracy. The scattering object has also been recovered in this case. However, the quantitative accuracy of the recovered anomalies is not as good with maximum values for absorption and scattering objects of 0.013 mm^{-1} and 1.3 mm^{-1}, respectively. This low quantitative accuracy has been reported elsewhere and is a common problem in 3D NIR imaging algorithms (Dehghani *et al* 2003b, Gibson *et al* 2003b), which may be solved using of multistage reconstruction algorithms (Srinivasan *et al* 2004) or with inclusion of *a priori* data (Brooksby *et al* 2003). Finally, using the correct model with correct information regarding the deformed boundary has produced images with very little or no artefacts.

6. Conclusions

In this work, we have presented a breast deformation model that would account for the change in shape and geometry of the breast due to the application of a circular array of optical fibres for NIR measurements. The proposed model, at present, assumes that the breast has homogenous mechanical properties, which, although not accurate, provide a good initial estimate for modelling of any deformation. Future studies may focus on using spatially distributed mechanical properties, as these can be imaged with good spatial resolution with MR elastography (Paulsen *et al* 1999, Van Houten *et al* 2000, Weaver *et al* 2001, Doyley *et al* 2003). Also, in this work, we have deformed the breast more than adequately needed by 19 mm, whereas in a real clinical setting, the deformation will be of lower magnitude, typically about 5–10 mm. In practice for our imaging exams, we currently attempt to deform the breast as minimally as possible, however, there are strategic benefits to compressing in that the signal transmitted can be higher, and there can be pressure-induced changes which might provide meaningful contrast about what the tissue is composed of (Jiang *et al* 2003). Nevertheless we have chosen such a large deformation to provide us with a worst-case scenario for NIR image reconstruction, and to examine if it is feasible to exploit larger magnitude deformations in clinical studies while not compromising the integrity of the data collected from the breast.

Using simulated data from the deformed breast that also contains optical anomalies, we have reconstructed images assuming various reconstruction geometries. In the first case of assuming that the reconstruction mesh is either a circular or irregular 2D mesh, the reconstructed images have shown good accuracy in recovering the location of the absorbing anomaly. The 2D reconstructed scattering images are not as good as expected, which is perhaps due to the fact that the scattering object had a small diameter of 15 mm and a contrast which was three times the background, and thus the image being dominated by boundary artefacts. Also it is evident from the reconstructed images that there exist large boundary artefacts which are due to the incorrect model. However, both the quality and quantitative accuracy of 2D image reconstruction will be improved by the incorporation of *a priori* information as well as a multi-step image reconstruction where regions of interest can be identified and isolated for regional reconstruction.

In the case of 3D image reconstruction, assumptions regarding the breast not being deformed might be used and the reconstructed images provide relatively good absorption distributions, but the images contain large artefacts which will likely confound their interpretation. The reason for this can be explained by considering the overall shape of the breast before and after deformation. The non-deformed mesh at the plane of measurement has radius that is 19 mm larger than the deformed mesh. Additionally, as evident from figures 1(a) and 1(b), it is found that the breast expands above, below and between each optical fibre once compressed. This large change in shape of the breast contributes to the large artefacts seen within the reconstruction. However, if one assumes that the diameter of the breast is known within the measurement plane, as well as an approximate diameter above and below it, it is possible to create a pseudo-3D conical shaped mesh for image reconstruction. Images reconstructed using this 3D conical mesh have shown a better accuracy in recovering both the absorbing and scattering anomalies. Finally, if accurate knowledge regarding the breast deformation is available, images of optical properties can be reconstructed which localize both anomalies with great accuracy, and also contain little or no artefact which otherwise would arise from model mismatch.

The goal of this work is to incorporate this new model of breast deformation with more accurate information regarding the mechanical properties of the breast to improve the NIR image reconstruction. The mechanical property information is readily available from other imaging modalities, and the synthesis of this information may provide fundamentally new information about breast physiologic response to pressure, and/or breast pathology response to pressure. An accurate model of breast deformation should in principle allow us to create patient specific models and meshes, which would in-turn provide more clinically useful data. Work is in progress to validate and further improve the deformation model with application to the female breast imaging.

Acknowledgments

This work has been sponsored by the National Cancer Institute through grants RO1CA69544 and PO1CA80139 and DOD Breast cancer research programme DAMD17-03-01-0405.

References

Arridge S R and Schweiger M 1995 Photon-measurement density functions. Part2: finite-element-method calculations *Appl. Opt.* **34** 8026–37

Arridge S R, Schweiger M, Hiraoka M and Delpy D T 1993 A finite element approach for modelling photon transport in tissue *Med. Phys.* **20** 299–309

Boas D A, Brooks D H, Miller E L, DiMarzio C A, Kilmer M, Gaudette R J and Zhang Q 2001 Imaging the body with diffuse optical tomography *IEEE Signal Process. Mag.* **18** 57–75

Brooksby B, Dehghani H, Pogue B W and Paulsen K D 2003 Infrared (NIR) tomography breast image reconstruction with *a priori* structural information from MRI: algorithm development for reconstructing heterogeneities *IEEE J. Sel. Top. Quantum Electron.* **9** 199–209

Dehghani H, Brooksby B, Vishwanath K, Pogue B W and Paulsen K D 2003a The effects of internal refractive index variation in near infrared optical tomography: a finite element modelling approach *Phys. Med. Biol.* **48** 2713–27

Dehghani H, Pogue B W, Jiang S, Brooksby B and Paulsen K D 2003b Three dimensional optical tomography: resolution in small object imaging *Appl. Opt.* **42** 3117–28

Dehghani H, Pogue B W, Poplack S P and Paulsen K D 2003c Multiwavelength three-dimensional near-infrared tomography of the breast: initial simulation, phantom, and clinical results *Appl. Opt.* **42** 135–45

Doyley M M, Meaney P M and Bamber J C 2000 Evaluation of an iterative reconstruction method for quantitative elastography *Phys. Med. Biol.* **45** 1521–40

Doyley M M, Weaver J B, Van Houten E E, Kennedy F E and Paulsen K D 2003 Thresholds for detecting and characterizing focal lesions using steady-state MR elastography *Med. Phys.* **30** 495–504

Eda H, Oda I, Ito Y, Wada Y, Oikawa Y, Tsunazawa Y, Tsuchiya Y, Yamashita Y, Oda M, Sassaroli A, Yamada Y and Tamaru M 1999 Multichannel time-resolved optical tomographic imaging system *Rev. Sci. Instrum.* **70** 3595–602

Fantini S, Franceschini M A, Gratton E, Hueber D, Rosenfeld W, Maulik D, Stubblefield P G and Stankovic M R 1999 Non-invasive optical mapping of the piglet in real time *Opt. Exp.* **4** 308–14

Fung Y C 1993 *Mechanical Properties of Living Tissue* (Berlin: Springer)

Galdino G M, Manson P N, Nahabedian M, Chang B, Zhuang P, Geng J Z and Vander Kolk C A 2002 Three dimensional photography in plastic surgery: clinical applications for breast surgery *Plastic Reconstr. Surg.* **110** 1–13

Geng Z 1996 Rainbow 3D camera—a new concept for high speed and low-cost 3D vision *J. Opt. Eng.* **35** 376

Gibson A, Riley J, Schweiger M, Hebden J c, Arridge S R and Delpy D T 2003a A method for generating patient specific finite element meshes for head modelling *Phys. Med. Biol.* **48** 481–95

Gibson A, Yusof R M, Hillman E M C, Dehghani H, Riley J, Everdale N, Richards R, Hebden J C, Schweiger M, Arridge S R and Delpy D T 2003b Optical tomography of a realistic neonatal head phantom *Appl. Opt.* **42** 1–8

Hebden J C, Veenstra H, Dehghani H H, Hillman E M C, Schweiger M, Arridge S R and Delpy D T 2001 Three dimensional time-resolved optical tomography of a conical breast phantom *Appl. Opt.* **40** 3278–87

Hillman E, Hebden J C, Schmidt F E W, Arridge S R, Schweiger M, Dehghani H and Delpy D T 2000 Calibration techniques and datatype extraction for time-resolved optical tomography *Rev. Sci. Instrum.* **71** 3415–27

Jiang H, Paulsen K D, Osterberg U L, Pogue B W and Patterson M S 1996 Optical image reconstruction using frequency-domain data: simulations and experiments *J. Opt. Soc. Am.* A **13** 253–66

Jiang S, Pogue B W, Paulsen K D, Kogel C and Poplack S P 2003 *In vivo* near-infrared spectral detection of pressure-induced changes in breast tissue *Opt. Lett.* **28** 1212–4

Krouskop T A, Wheeler T M, Kallel F, Garra B S and Hall T 1998 Elastic moduli of breast and prostate tissues under compression *Ultrason. Imaging* **20** 260–74

McBride T O, Pogue B W, Jiang S, Osterberg U L, Paulsen K D and Poplack S P 2002 Multi-spectral near-infrared tomography: a case study in compensating for water and lipid content in haemoglobin imaging of the breast *J. Biomed. Opt.* **7** 72–9

McBride T O, Pogue B W, Osterberg U L and Paulsen K D 2003 Strategies for absolute calibration of near infrared tomographic tissue imaging *Oxygen Transport Tissue XXIV* (Dordrecht: Kluwer) pp 85–99

Paulsen K D, Miga M I, Kennedy F E, Hoopes P J, Hartov A and Roberts D W 1999 A computational model for tracking subsurface tissue deformation during stereotactic neurosurgery *IEEE Trans. Biomed. Eng.* **46** 213–25

Pogue B W, Geimer S, McBride T O, Jiang S, Österberg U L and Paulsen K D 2001 Three-dimentional simulation of near-infrared diffusion in tissue: boundary condition and geometry analysis for finite element image reconstruction *Appl. Opt.* **40** 588–600

Pogue B W and McBride T *et al* 1999 Comparison of imaging geometries for diffuse optical tomography of tissue *Opt. Exp.* **4** 270–86

Schoberl J *NETGEN—An Automatic 3D Tetrahedral Mesh Generator* http://www.sfb013.uni-linz.ac.at/~joachim/netgen/

Schweiger M and Arridge S R 1999 Optical tomographic reconstruction in a complex head model using *a priori* region boundary information *Phys. Med. Biol.* **44** 2703–22

Schweiger M, Arridge S R, Hiroaka M and Delpy D T 1995 The finite element model for the propagation of light in scattering media: boundary and source conditions *Med. Phys.* **22** 1779–92

Srinivasan S, Pogue B W, Dehghani H, Jiang S, Song X and Paulsen K D 2004 Improved quantification of small objects in near-infrared diffuse optical tomography *J. Biomed. Opt.* at press

Timoshenko S P and Goodier J N 1970 *Theory of Elasticity* (Singapore: McGraw-Hill)

Van Houten E E, Weaver J B, Miga M I, Kennedy F E and Paulsen K D 2000 Elasticity reconstruction from experimental MR displacement data: initial experience with an overlapping subzone finite element inversion process *Med. Phys.* **27** 101–7

Weaver J B, Van Houten E E, Miga M I, Kennedy F E and Paulsen K D 2001 MR elastography using 3D gradient echo measurements of steady state motion *Med. Phys.* **28** 1620

APPENDIX 2

Breast Deformation in Near Infrared Optical Tomography

Hamid Dehghani[1], Brian W. Pogue[1], Marvin M. Doyley[2], Jason Geng[3] and Keith D. Paulsen[1]
[1]*Thayer School of Engineering, Dartmouth College, Hanover, NH 03755*
[2]*Department of Radiology, Dartmouth Medical School, Hanover, NH 03755*
[3]*Genex Technologies, Inc. 10605 Concord Street, Suite 500, Kensington, MD 20895-2504*
email:dehghani@dartmouth.edu, Tel:(603) 646-9193, Fax:(603) 646-3856

Abstract: In NIR tomography of the breast, good contact is needed by the fibers, resulting in breast deformation. We present a deformation model to account for the change of shape and discuss implications in image reconstruction.

©2004 Optical Society of America

OCIS codes: (170.3830) Mammography; (170.6960) Tomography; (100.3010) Image reconstruction techniques; (100.3190) Inverse problems

1. Introduction

Near Infrared (NIR) tomography is an emerging alternative imaging method used to image physiologic parameters of biological tissue in-vivo such as water and hemoglobin [1]. Measurements of light propagation (600 – 900 nm) within tissue can be used to map internal chromophore concentrations within tissue. Light is transmitted through tissue using multiple input and output locations on the surface of the region to be imaged using optical fibers for delivery and pickup of the light signals. To obtain clinical measurements with a sufficient signal to noise ratio, it is key to ensure good contact exists between the optical fibers and the tissue. The breast is a soft tissue, which will deform and alter its shape on the application of external pressure. The amount of deformation is a function of the tissue mechanical properties and the amount of displacement and the external pressure applied by the optical fiber array. In most image reconstruction algorithms, the general assumption is made that the region under investigation is a uniform circular (2D) or conical or cylindrical (3D) domain [2]. Little work has been done to evaluate the effect of any incorrect geometry in image reconstruction. In this work, the effect of such assumptions is investigated by creating a deformation of the breast model in 3D to generate stimulated clinical data. Images are then reconstructed using various assumptions regarding the imaging domain such as 3D conical shaped models and the non-deformed breast model to evaluate image quality.

2. Methods

Soft tissues exhibit nonlinear elastic behavior. Nevertheless, they can be considered a linear elastic material in situations where the deforming forces produce infinitesimal deformations (i.e. ≤ 5 %). For the purpose of this study, the breast was modeled as linear isotropic pseudo-incompressible medium (i.e. Poisson's ratio (ν)= 0.495). Under these assumptions and ignoring internal body force, the governing elasticity equations for quasi-static deformation is given by:

$$(\lambda+\mu)\nabla(\nabla\cdot\vec{u})+\mu\nabla^2\vec{u}=0 \qquad \text{for internal nodes in domain } \Omega \qquad (1)$$

$$\left((\lambda+\mu)\nabla(\nabla\cdot\vec{u})+\mu\nabla^2\vec{u}\right)\hat{n}=h \qquad \text{for nodes on the boundary } \delta\Omega. \qquad (2)$$

Here $\hat{n}$ represents a unit vector directed outwards from Ω, and h represents the traction on the surface or boundary of the breast. Note that $\vec{u}$ represents the displacement components in all coordinate directions, and μ and λ are Lame's elastic constants. For an isotropic medium these constants are related to the more familiar Young's modulus (E) and the Poisson's ratio (ν) by $\mu=\frac{E}{2(1+\nu)}$ and $\lambda=\frac{\nu E}{(1+\nu)(1-2\nu)}$.

It should be stated that in this study the breast was assumed to be traction free and internal body forces were neglected, thus the problem was solved by imposing a prescribed displacement [3]. A volume mesh of a female breast of a volunteer was created from surface image data that was acquired using a 3D surface camera [Rainbow 3D Camera, Genex Technologies, Kensington MD]. The 3D camera projects structural illumination patterns onto the object and calculates 3D surface profile described by over 300,000 data points [4]. A volume mesh was then generated using the Delaunay algorithm. The mesh has a geometry of 130 x 136 x 60 mm, Figure 1(a) and contained 15501 nodes corresponding to 61171 linear tetrahedral elements. The diameter of the breast at its mid-plane where optical fiber array would be applied is approximately 88 mm. To calculate the deformation due to 16 equally spaced optical fibers being applied at the mid-plane of the breast, i.e. $z = -30$ mm, it is assumed that each optical fiber pushed the breast so that the final breast diameter at $z = -30$ mm is 70 mm, and that the diameter of each optical fiber is 6 mm. The modeled elastic properties of tissue, were assumed as isotropic and homogenous with Young's Modulus of 20 kPa and Poisson's ratio of 0.495. Further, it was assumed that the top most part of the mesh, i.e. $z = 0$ mm was not allowed to move since it is connected to the chest. Using this applied displacement as a boundary condition, the displacement at all nodes due to the application of the optical fibers was calculated and a deformed mesh was created, Figure 1(b).

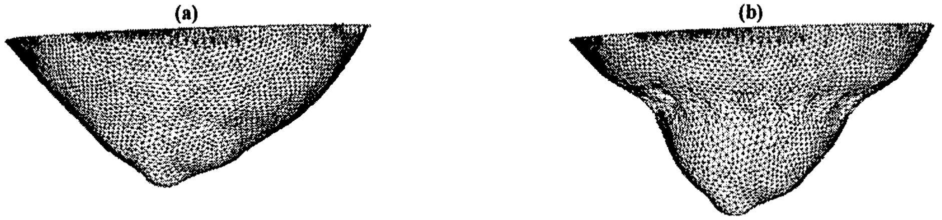

Figure 1. Volume mesh is shown of the (a) normal suspended breast and (b) the deformed mesh after the application of the optical fiber array.

In order to accurately simulate the clinical settings, two localized anomaly regions were placed within the mid-plane of the normal breast, both at $z = -30$ mm, Figure 2(a). First was an absorbing anomaly, 19 mm from the surface and a radius 10 mm with a coefficient value of 0.03 mm^{-1}. Second was a reduced scattering anomaly, also 19 mm from the surface but with a radius of 7.5 mm and a value of 3 mm^{-1}. The background optical properties were modeled with an absorption coefficient of 0.01 mm^{-1} and a reduced scatter coefficient of 1.0 mm^{-1}. For the deformed breast model the same optical properties of the normal breast, including the anomalies were assumed. Once the deformation of the model was calculated, it was assumed that the anomalies were free to move, depending on the elastic properties of the breast, Figure 2(b).

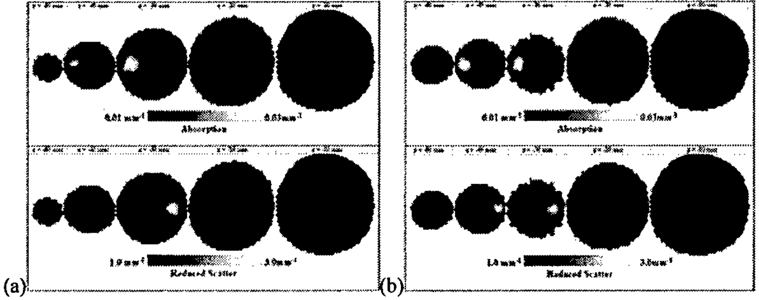

Figure 2. 2D coronal slices through (a) the normal breast mesh and (b) the deformed breast mesh, showing the position of the anomalies. The right hand slice is near the chest while the most left hand slice is near the nipple.

Using the deformed mesh, together with the displaced anomalies, NIR data were simulated for 16 equally circularly spaced optical fibers placed at $z = -30$ mm. Amplitude and phase data were simulated at 100 MHz, and 1% noise were added. This data was then used as simulated patient data in the following sections. In addition, to allow data calibration as done using clinical data, and discussed elsewhere [2], the data was simulated for 16 equally spaced optical fibers placed in a circle around the mid-plane of a cylindrical model with homogenous background optical properties.

3. Results

Assuming that correct anatomical information regarding the breast is available, before application of the optical fiber array, the normal, non-deformed mesh was used, Figure 1(a), during reconstruction to produce the images shown in Figure 3(a). Also, images reconstructed assuming a conical shaped breast (diameter at $z = -30$ set to equal the diameter of the optical fiber array) are shown in Figure 3(b). Finally, to show the best possible reconstruction, the deformed mesh was used for reconstruction of images and these results are shown in Figure 3(c).

From images reconstructed using the correct but non-deformed breast, although the absorbing anomaly has been recovered, the reduced scattering images contain large artifacts. The background absorption and scatter values are about 0.006 mm^{-1} and 0.5 mm^{-1} respectively, while the maximum absorption for the anomaly is 0.014 mm^{-1}. In images assuming a conical model the background absorption and scatter values are about 0.007 mm^{-1} and 0.94 mm^{-1}

respectively, while the maximum absorption for the anomaly is 0.014 mm^{-1}. Here, although the target values are better quantitatively, the images contain artifacts, are much smaller, and the absorption scatter cross-talk is more than expected. In images reconstructed assuming correct 3D deformed boundary, both the absorbing and scattering regions have been recovered with improved localization accuracy. Some cross talk exists between the absorbing and scattering anomalies. The background absorption and scatter values are about 0.01 mm^{-1} and 0.98 mm^{-1} respectively, while the maximum absorption and scatter values for the anomalies are 0.013 mm^{-1} and 1.3 mm^{-1} respectively. It is important to note that although the images in Figure 3(a) show a better quantitative accuracy for the recovered absorbing anomalies, the background values are much lower than expected and the images contain far more artifacts.

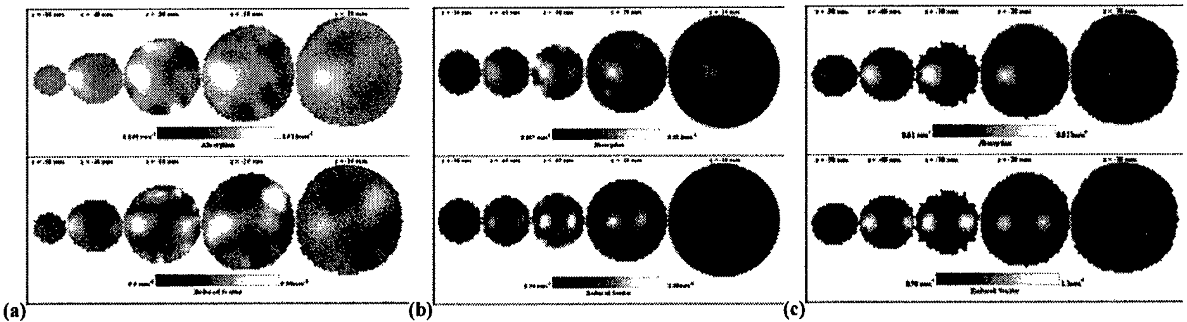
(a) (b) (c)

Figure 3. 3D simultaneous reconstruction of absorption and reduced scatter from deformed breast model simulated data are shown. The mesh used for the reconstruction was (a) the normal un-deformed breast; (b) conical mesh and (c) the correct deformed breast. The most right hand slice is near the chest while the most left hand slice is near the nipple in each set of images.

4. Discussion

In the case where it is assumed that the exact breast geometry is known, but the details of the fibers compression have been ignored, although the absorption anomaly was recovered with relatively good accuracy, the reduced scattering image contains a large artifact. Furthermore, the calculated background values for absorption and scatter are 0.006mm^{-1} and 0.5 mm^{-1} respectively, which are much lower than expected. These images are, perhaps, not as accurate and useful as the conical geometry case, since, although there is a more accurate 3D model, the diameter of the breast was not correct, particularly within the measurement plane, i.e. $z = -30$ mm. When using the geometrically correct deformed mesh to reconstruct images of absorption and scatter, superior localization accuracy resulted. The scattering object has also been recovered in this case. However, the quantitative accuracy of the recovered anomalies is not as good with maximum values for absorption and scatter of 0.013mm^{-1} and 1.3 mm^{-1}, respectively. This modest degradation in quantitative accuracy has been reported elsewhere and is a common problem in 3D imaging algorithms, which may be solved through the use of multi-stage algorithms [5] or with inclusion of a priori data. Nonetheless using the correct model with correct information regarding the deformed boundary has produced images with very little to no artifacts.

5. Acknowledgements

This work has been sponsored by the National Cancer Institute through grants RO1CA69544 and PO1CA80139 as well as DOD Breast cancer research program DAMD17-03-01-0405.

6. References

1. McBride, T.O., Pogue B W , S. Jiang, U. L. Osterberg, K. D. Paulsen, and S. P. Poplack, *Multi-spectral near-infrared tomography: a case study in compensating for water and lipid content in hemoglobin imaging of the breast.* J. Biomed. Opt., 2002. 7.
2. Dehghani, H., Pogue, B. W., Poplack, S. P., Paulsen, K. D., *Multiwavelength Three-Dimensional Near-Infrared Tomography of the Breast: Initial Simulation, Phantom, and Clinical Results.* Applied Optics, 2003. **42**(1): p. 135-145.
3. Doyley, M.M., Meaney, P. M., and Bamber, J. C., *Evaluation of an iterative reconstruction method for quantitative elastography.* Phys. Med. Biol., 2000. **45**(6): p. 1521-1540.
4. Geng, Z., *Rainbow 3D Camera - A New Concept for High Speed and Low-Cost 3D Vision.* Journal Optical Engineering, 1996. **35**(2): p. 376.
5. Srinivasan, S., Pogue, B. W., Dehghani, H., Jiang, S., Song, X., and Paulsen, K. D., *Improved Quantification of Small Objects in Near-Infrared Diffuse Optical Tomography.* J. Biomed. Opt., 2003. **Submitted**.

Spectrally-Constrained Chromophore and Scattering Reconstruction for In Vivo NIR Tomography

Subhadra Srinivasan, Brian W. Pogue, Shudong Jiang,
Hamid Dehghani, Keith D. Paulsen
Thayer School of Engineering, Dartmouth College, Hanover, NH 03755
(Email: subha@dartmouth.edu, Tel:(603) 646-2859, Fax:(603) 646-3856)

Abstract

A multi-spectral direct chomophore and scattering reconstruction technique has been implemented for near-infrared frequency-domain tomography in recovering images of total hemoglobin, oxygen saturation, water and scatter parameters. The method applies the spectral-constraint of the chromophores and scattering spectra into the inversion algorithm, thereby reducing the parameter-space of the inversion process. This new method was validated in experimental phantoms and clinical images. Analysis of the recovered images indicates that the added spectral-constraint in the inversion allows a lower level of regularization to be used to achieve the same minimization error norm in the objective function. This approach also produces a significant reduction in image artifacts and is improved in image accuracy.

Near Infra-Red (NIR) tomography is known for its ability to distinguish between malignant and normal tissue based on a high-contrast mechanism arising from intrinsic processes such as angiogenesis and hypoxia. Absorption-based parameters can be recovered such as total hemoglobin, oxygen saturation and water fraction as well as elastic scattering. These can provide measures of physiology or pathophysiology related to the intravascular and extravascular spaces as well as the composition of tissue. In-vivo studies have demonstrated levels of hemoglobin in tumors over twice that in normal breast [1, 2]; however, one of the current challenges is to optimize the quantitative accuracy with which these parameters can be determined. Typically, spectral tomography approaches make use of sparse data at discrete wavelengths instead of a complete spectrum. This sparse spectral sampling coupled with an image reconstruction process which is ill-posed, amplifies errors in quantifying the physiological parameters of the tissue.

The method illustrated here reduces noise in the recovery of chromophores, especially significant in water and scattering, by eliminating the need to reconstruct the absorption and scattering coefficients as intermediate endpoints. Instead, the chromophore concentrations and scatter parameters are estimated directly by incorporating the known Beer's law relation and Mie scattering behavior as constraints. Corlu et al [3] have implemented this approach using continuous wave measurements to find the optimal four wavelengths that reduce the crosstalk between absorption and scatter parameters. Their results from simulations are encouraging under the assumption that all change in scattering is due to scatter amplitude with scatter power kept constant. A similar approach to CW data has been implemented by Li et al[4] who have used two of three wavelengths under the assumption that there is no scattering perturbation. They have applied this method to find chromophore concentrations directly, and have shown in simulated and experimental data that their technique results in reduced artifacts and crosstalk. In this study, we extend the approach to application of full frequency-domain data sets at six wavelengths, and demonstrate reconstruction in phantoms and humans. The method uses a finite element model of the diffusion equation and reconstructs images for five parameters: oxyhemoglobin, hemoglobin, water fraction, scatter amplitude and scatter power, with no assumptions on scatter amplitude or power. The results, in addition to showing a reduction in noise in the recovered chromophore concentrations, also provide evidence of improvement in image accuracy and suppression of image artifacts.

The NIR frequency domain imaging system (tailored for breast imaging) has been described in detail elsewhere [5]. Briefly, it consists of optical fibers placed in three planes in a circular geometry. Each plane has 16 source-detector positions and intensity modulated light at 100MHz is used at six different wavelengths in the range 660-850nm. The signal amplitude and phase is calibrated to compensate for system offsets by matching measured data from homogeneous calibration phantoms to simulated results from the finite element model.

Image reconstruction uses Newton's method to iteratively solve for the optical properties where the underlying model is a finite element solution of the diffusion approximation to the radiative transfer equation and appropriate boundary conditions have been applied (type III-Robin type boundary). Further details can be found in [6]. In simple terms, this iterative procedure involves the Taylor series approximation:

$$\partial\phi = \Im\partial\mu \, , \tag{1}$$

where $\partial\phi$ refers to the change in boundary data, $\Im$ is the Jacobian, the matrix containing the sensitivity of the boundary data to change in optical properties, $\Im = [\Im_{\mu_a}, \Im_{\kappa}]$; and $\partial\mu$ is the update in the optical properties given by $\partial\mu = (\partial\mu_a, \partial\kappa)$ where μ_a is the absorption coefficient in mm^{-1} and κ is the diffusion coefficient given by $\kappa = \frac{1}{3(\mu_a + \mu_s^{'})}$ in mm, and $\mu_s^{'}$ is the reduced scattering coefficient in mm^{-1}. The inverse problem corresponding to equation (1) is solved with application of the Levenberg-Marquardt regularization scheme for stabilization. Previously, the optical properties at each wavelength were obtained, and then the calculation of the chromophore concentrations was performed in a single step using the linear relation

$$\mu_a = [\varepsilon]c \tag{2}$$

where ε is the molar absorption spectra of the tissue absorbing chromophores, in our case, oxy-hemoglobin (HbO2), hemoglobin (Hb) and water; and c is the concentration of these chromophores. Similarly, for scattering the approximation to Mie theory [7, 8],

$$\mu_s' = a\lambda^{-b} \tag{3}$$

was used to derive scatter amplitude (*a*) and scatter power (*b*) with wavelength in µm. Assuming that we know $\Im_\mu = \frac{\partial\phi}{\partial\mu}$ and $\Im_\kappa = \frac{\partial\phi}{\partial\kappa}$ as calculated by the previous method, in the new approach the measurements at all wavelengths are coupled together, and the relationships in equations 2 and 3 are combined to create a new set of equations, which for each wavelength, is represented by:

$$\partial\phi_\lambda = \Im_{c,\lambda}dc + \Im_{a,\lambda}da + \Im_{b,\lambda}db \tag{4}$$

where

$\Im_{c,\lambda} = \frac{\partial\phi}{\partial c}\Big|_\lambda = \frac{\partial\phi}{\partial\mu}.\frac{\partial\mu}{\partial c}\Big|_\lambda$, for each chromophore in the model. From equation 2, we get $\partial\mu = \varepsilon\partial c$, so that, substituting for $\frac{\partial\mu}{\partial c}$,

$$\Im_{c,\lambda} = \frac{\partial\phi}{\partial c}\Big|_\lambda = \frac{\partial\phi}{\partial\mu}\varepsilon\Big|_\lambda = \left(\frac{\partial\phi}{\partial\mu}\Big|_\lambda\right) \otimes \left(\varepsilon_\lambda^{c1,c2,c3}\right) = \Im_{\mu,\lambda} \otimes \left(\varepsilon_\lambda^{c1,c2,c3}\right) \tag{5}$$

where ⊗ refers to the Kronecker tensor product.

Similarly, expressions for $\Im_{a,\lambda}$ and $\Im_{b,\lambda}$ can be derived, and come out to be

$$\Im_{a,\lambda} = \frac{\partial\phi}{\partial a} = \frac{\partial\phi}{\partial\kappa}.\frac{\partial\kappa}{\partial a}\Big|_\lambda = \Im_\kappa\left(-3\kappa^2\right)\left(\lambda^{-b}\right)\Big|_\lambda \tag{6}$$

Similarly, for the scatter power b part:

$$\Im_{b,\lambda} = \Im_{\kappa}\left(-3\kappa^{2}\right)\left(\mu_{s}^{'}\right)\left(-\ln\lambda\right)\Big|_{\lambda} \tag{7}$$

The overall system of equations is built by substituting the relations from (5), (6) and (7) into equation 4:

$$\begin{pmatrix} \partial\phi_{\lambda 1} \\ \partial\phi_{\lambda 2} \\ .. \\ \partial\phi_{\lambda n} \end{pmatrix} = \begin{bmatrix} \Im_{c1,\lambda 1}\Im_{c2,\lambda 1}\Im_{c3,\lambda 1}\Im_{a,\lambda 1}\Im_{b,\lambda 1} \\ \Im_{c1,\lambda 2}\Im_{c2,\lambda 2}\Im_{c3,\lambda 2}\Im_{a,\lambda 2}\Im_{b,\lambda 2} \\ \ldots\ldots \\ \Im_{c1,\lambda n}\Im_{c2,\lambda n}\Im_{c3,\lambda n}\Im_{a,\lambda n}\Im_{b,\lambda n} \end{bmatrix} \begin{pmatrix} \partial c_1 \\ \partial c_2 \\ \partial c_3 \\ \partial a \\ \partial b \end{pmatrix} \tag{8}$$

The size of the left hand vector is number of wavelengths times number of measurements per wavelength while the size of the right hand side vector is number of chromophores times number of nodes for updating each chromophore in the mesh. The individual Jacobians for each chromophore were computed using a dual mesh technique [9], on a 2000 node mesh for forward diffusion calculations and a 425 node mesh for image reconstruction. Equation 8 was implemented by building up the new Jacobian (5x425 by 480x6). The same Levenberg-Marquardt regularization scheme was applied and the computation time was approximately 25minutes for typically 5-7 iterations; the measure of convergence being when the difference between measured and calculated data (projection error) was less than 2% of previous iteration value.

In order to test the accuracy of the reconstruction procedure with experimental measurements, data was collected on a liquid tissue-simulating phantom within a plastic circular container consisting of 1% Intralipid and 1% blood in buffered saline. The blood hematocrit was measured before the experiment by a clinical co-oximeter that showed 1% whole blood was equivalent to 17μM of hemoglobin; and water is expected to be 100%. Measurements were carried out on this phantom in fully oxygenated and deoxygenated states, with the latter done by reducing pO_2 in the phantom through the addition of yeast. Figure 1 shows the mean and standard deviation from recovered images for total hemoglobin (Hb_T), oxygen saturation (S_tO_2), water fraction and scatter parameters by both spectrally-constrained approach and the former method where each wavelength is reconstructed separately. The mean recovered Hb_T, S_tO_2 and water fraction values are accurate with less than 3% mean error for spectral method and 5.1% for the separate wavelength reconstruction using the stopping criterion of less than 2% projection error change between iterations. The error bars in the figure show the standard deviation in the homogeneous images; the standard deviations in the spectrally-constrained images are much lower than those from the conventional technique. The images were not spatially-filtered in either method, so that no averaging of properties occurred in order to preserve maximum quantitative accuracy. The reconstruction by spectral method converges at iteration 6, and is ~12 iterations for conventional technique, for each wavelength. Reduced standard deviation in the old technique can be achieved by artificially stopping the reconstruction before the convergence criterion; the standard deviation using iteration 6 for conventional technique is shown in Figure 1, and is lower than obtained by letting the conventional reconstruction converge till projection error changes by less than 2%. Reduced standard deviation in the conventional technique can also be achieved by the use of filtering, with the tradeoff in quantitative damping of optical properties; whereas the spectral technique offers lower noise in images without using filters. The reduction in standard deviation is especially significant in water fraction and scattering parameters and artifacts occurring close to the boundary in the images have been suppressed using the spectral approach. The spectral reconstruction technique was also applied to the complete set of 16 measurement sets obtained for varying pO_2 measured separately by a chemical microelectrode. The recovered oxygen saturation follows the predicted Hill curve with a mean error of 7.7% (data not shown).

To evaluate the spectrally-constrained method with heterogeneous experimental data, a similar liquid phantom as above was constructed with 1% intralipid and 1% pig blood (measured to be ~0.017mM) in buffered saline in a 90mm diameter plastic bottle. A clear plastic cylindrical inclusion of diameter 20mm was placed at 10 o'clock in the phantom 10mm from the edge with the same Intralipid solution but twice the concentration of blood (2% = 0.034 mM). Amplitude and phase measurements were obtained in the frequency domain at six wavelengths and the images were reconstructed by applying both the spectral and conventional two-stage method, as shown in Figure 2. Recovered images from the direct approach are shown in the top row and were obtained with the stopping criterion of less than 2% error change between iterations (7 iterations). This technique converges faster than the conventional two-stage method. The corresponding images obtained by using absorption and scatter estimates at the seventh iteration from the conventional method are shown in middle row of Figure 2 while those images based on the same projection error change criterion for each wavelength appear in the bottom row. The direct chromophore reconstruction shows quantitatively accurate property recovery with 8% error in Hb_T and less than 2% error in S_tO_2 and water fraction, in the region of interest. The images in the top and middle row are comparable; however, the images from the middle row show an artifact developing in the center, which is more pronounced in the bottom row when the same stopping criterion is applied. The images are expected to be homogeneous in all other parameters except total hemoglobin. The water fraction and scattering images in particular show lower noise in the spectral reconstruction. Some inhomogeneity is observed in the water fraction images, which results from the walls of the plastic inclusion. No filtering has been applied to any of the images, and some artifacts are observable close to the edges in certain images, which may be due to the boundary of the plastic phantom. In general, the coupling of all measured wavelengths to reconstruct chromophores and scattering directly appears to suppress the common noise components within the individual datasets, leading to more artifact free images.

The direct spectral reconstruction method has also been applied to clinical tomography data obtained from measurements on a 66 year old subject with a 5-10 mm spiculated mass evident on mammography, which was later diagnosed as Invasive Ductal Carcinoma. The subject underwent the NIR exam in accordance with the Dartmouth protocol, where informed consent was obtained prior to the exam. The position of the anomaly was provided through mammography and determined to be at 11:30 o'clock in the cranocaudal view and located about 1cm from surface. NIR data was collected in three planes. Reconstructed images are shown in Figure 3 for the plane in line with the tumor. A localized increase in Hb_T was observed and the contrast available was 1.7:1.0 in tumor versus background. The S_tO_2 image showed a decrease at the location of the tumor with a contrast of 0.7:1. The corresponding S_tO_2 image with the conventional technique (not shown) was noisier, and a similar decrease was not observed. The water fraction image showed heterogeneity in the range 0.25 to 0.5%, which is considerably smaller than the range of 0 to 1% observed with the old method. Tighter data ranges are similarly observed in the scatter images, and artifacts evident in the separate wavelength technique have been suppressed in the spectral approach.

In summary, the new direct spectral reconstruction technique has been applied to homogeneous and heterogeneous data and the results have consistently reduced artifacts as well as improved quantitative accuracy in recovered parameters. With this new technique, higher hemoglobin content at the site of tumor is observed in the clinical case, as well as lower oxygen saturation. The water fraction and scattering images show the most significant improvement in all cases by reduction of the image artifacts.

This work has been supported through NIH grants PO1CA80139 and RO1CA69544 and Department of Defense DAMD17-03-01-0405. The authors would like to acknowledge expert clinical collaboration with Steven P.Poplack, Sandra K. Soho and Christine Kogel.

Figure Captions

Figure 1. Mean and standard deviations from images of Hb_T [mM], S_tO_2 [%], water fraction, 100xa and 100xb for the spectral approach using convergence criterion of projection error variation less than 2% between iterations (converges at iteration 6); for the conventional method using corresponding 6th iteration values and for the conventional method using the convergence criterion as applied for spectral method (converges at ~12 iterations for each wavelength). These were generated from experimental measurements on a homogeneous phantom containing 17μM whole blood with 1% Intralipid in saline.

Figure 2. Reconstructed images of Hb_T [mM], S_tO_2 [%], water fraction, 'a' and 'b' parameters from experimental data on a phantom solution of Intralipid in saline with 0.017 mM hemoglobin in background and 0.034 mM in the heterogeneity. Images with the spectral approach are shown in row 1 using a stopping criterion of projection error variation being less than 2% (~7 iterations). Row 2 shows the conventional method after 7 iterations, and row 3 shows the old method using the same stopping criterion as row 1 (10-12 iterations for each wavelength).

Figure 3. Hb_T [mM], S_tO_2 [%], water fraction, 'a' and 'b' images are shown from measurements on a cancer subject with a 5-10 mm Invasive Ductal Carcinoma at the 11:30 clock face position.

Figure1

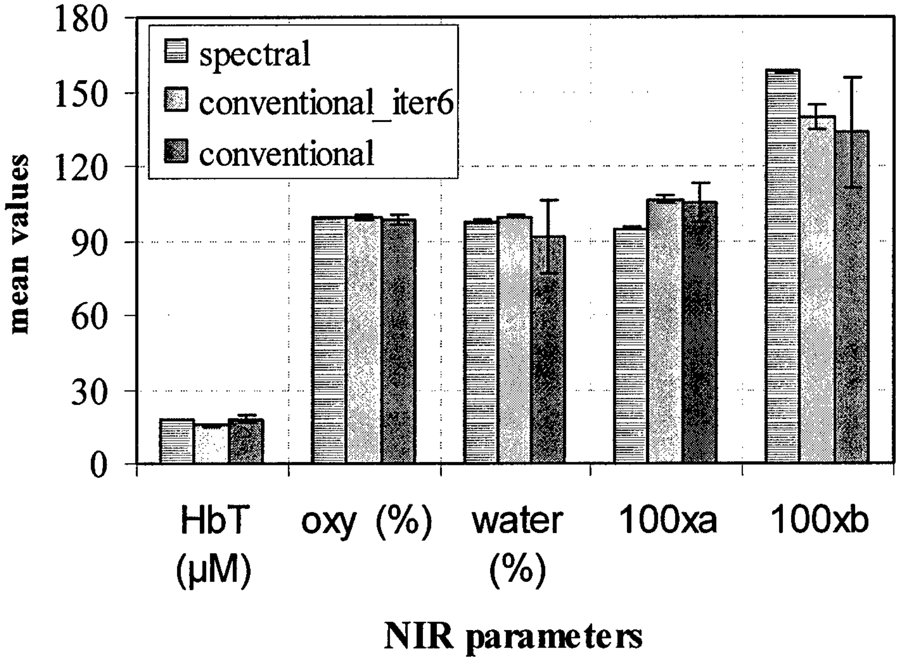
180
150
120
90
60
30
0
mean values
spectral
conventional_iter6
conventional
HbT (μM)
oxy (%)
water (%)
100xa
100xb
NIR parameters

Figure2

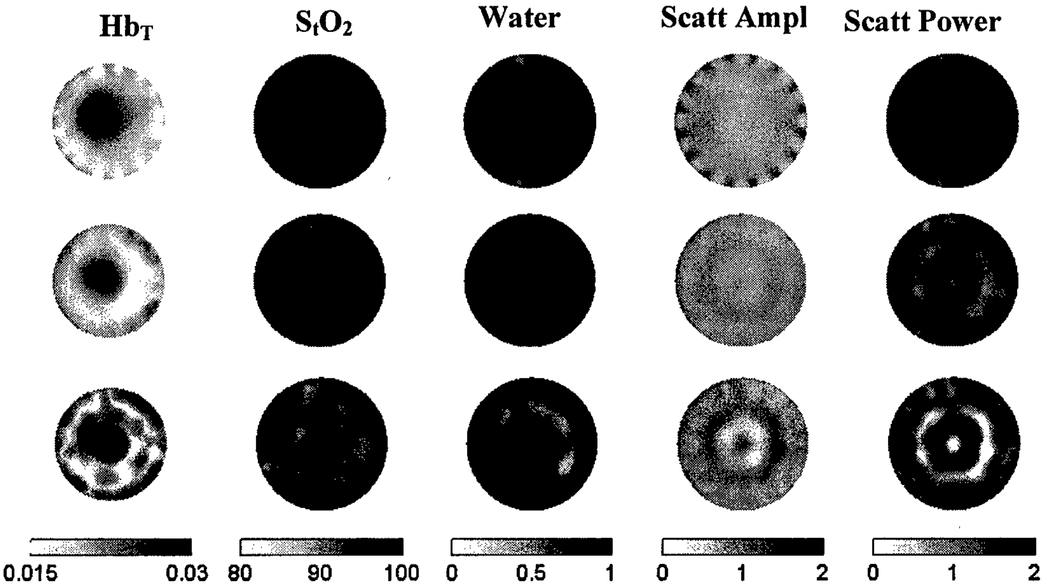

HbT
StO2
Water
Scatt Ampl
Scatt Power
0.015
0.03
80
90
100
0
0.5
1
0
1
2
0
1
2

Figure 3

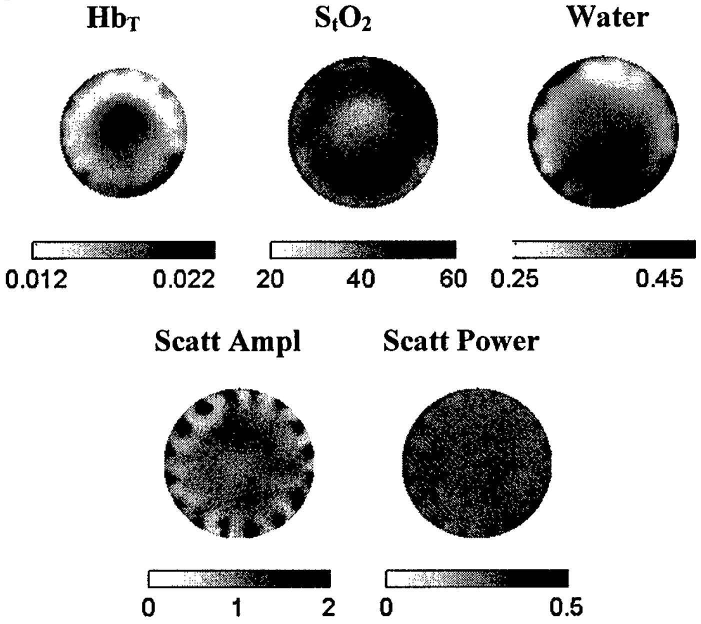

Hb_T S_tO_2 Water

Scatt Ampl Scatt Power

0.012
0.022
20
40
60
0.25
0.45
0
1
2
0
0.5

References

1. B.W. Pogue, S.P. Poplack, T.O. McBride, W.A. Wells, O.K. S., U.L. Osterberg, and K.D. Paulsen, "Quantitative Hemoglobin Tomography with Diffuse Near-Infrared Spectroscopy: Pilot Results in the Breast." *Radiology*, vol. 218(1) pp. 261-6.2001.
2. B.J. Tromberg, N. Shah, R. Lanning, A. Cerussi, J. Espinoza, T. Pham, L. Svaasand, and J. Butler, "Non-invasive in vivo characterization of breast tumors using photon migration spectroscopy." *Neoplasia (New York)*, vol. 2(1-2) pp. 26-40.2000.
3. A. Corlu, T. Durduran, R. Choe, M. Schweiger, E.M. Hillman, S.R. Arridge, and A.G. Yodh, "Uniqueness and wavelength optimization in continuous-wave multispectral diffuse optical tomography." *Opt Lett*, vol. 28(23) pp. 2339-41.2003.
4. A. Li, Q. Zhang, J.P. Culver, E.L. Miller, and D.A. Boas, "Reconstructing chromosphere concentration images directly by continuous-wave diffuse optical tomography." *Opt Lett*, vol. 29(3) pp. 256-8.2004.
5. T.O. Mcbride, Pogue,B. W., Jiang, S., Osterberg, U. L., Paulsen, K. D., "A parallel-detection frequency-domain near-infrared tomography system for hemoglobin imaging of the breast in vivo." *Review of Scientific Instruments*, vol. 72(3) pp. 1817-1824.2001.
6. K.D. Paulsen, and Jiang H., "Spatially varying optical property reconstruction using a finite element diffusion equation approximation." *Med. Phys.*, vol. 22(6) pp. 691-701.1995.
7. H.J. van Staveren, Moes, C. J. M., van Marle, J., Prahl, S.A. and van Gemert, J. C., "Light scattering in Intralipid - 10% in the wavelength range of 400-1100nm." *Applied Optics*, vol. 30(31) pp. 4507-4514.1991.
8. J.R. Mourant, Fuselier, T., Boyer, J., Johnson, T. M., and Bigio, I. J., "Predictions and measurements of scattering and absorption over broad wavelength ranges in tissue phantoms." *Applied Optics*, vol. 36(4) pp. 949-957.1997.
9. K.D. Paulsen, Meaney, P. M., Moskowitz, M. J. and Sullivan, J. M., "A dual mesh scheme for finite element based reconstruction algorithms." *IEEE Trans Med Imaging*, vol. 14(3) pp. 504-514.1995.

Magnetic Resonance-Guided Near-Infrared Tomography of the Breast

Ben Brooksby[1], Shudong Jiang[1], Christine Kogel[2], Marvin Doyley[1], Hamid Dehghani[1], John B. Weaver[2], Steven P. Poplack[2], Brian W. Pogue[1], and Keith D. Paulsen[1]

[1] *Thayer School of Engineering, Dartmouth College, Hanover NH 03755*

[2] *Department of Diagnostic Radiology, Dartmouth Medical School, Hanover NH 03755*

ABSTRACT

The design and implementation of a multi-spectral, frequency-domain near infrared tomography system is outlined, which operates in an MRI magnet for utilization of MR-guided image reconstruction of tissue optical properties. Using long silica optical fiber bundles, measurements of light transmission through up to 12 cm of female breast tissue can be acquired simultaneously with MRI scans. The NIR system utilizes six optical wavelengths from 660-850 nm using intensity modulated diode lasers nominally working at 100 MHz. Photomultiplier tube detector gain levels are electronically controlled on a time scale of 200 ms, thereby allowing rapid switching of the source to locations around the tissue. There are no moving parts in the detection channels and for each source position, 15 PMTs operating in parallel allow sensitivity down to 0.5 pW/cm^2 at the tissue surface. Images of breast tissue optical absorption and reduced scattering coefficients are obtained using a Newton-type reconstruction algorithm to solve for an optimal solution using the measurement data. In medical imaging, it is beneficial to compare the same tissue volume as seen by a variety of modalities, and perhaps more importantly, there is the hypothesis that one imaging system which has high spatial resolution can be used to enhance the reconstruction of another system which has good contrast resolution. In this study we explore the synergistic benefits of a combined NIR-MRI data set, specifically the ways in which MRI (i.e. high spatial resolution) enhances NIR (i.e. high contrast resolution) image reconstruction. The design, calibration, and performance of the imaging system are described in the context of preliminary phantom tests and initial *in vivo* patient imaging.

I. INTRODUCTION

Diffuse optical tomography (DOT) with near infrared (NIR) light can be used to produce spatially resolved images of tissue optical properties. These optical property maps can be acquired at different wavelengths and combined to reveal hemoglobin concentration, oxygen saturation, water and fat content, as well as a description of scattering structures[1-5]. These latter parameters are important indicators of metabolic activity, functional processes, or presence and staging of disease. NIR diffuse tomography generally suffers from comparatively low spatial resolution due to the multiple scattering events that occur along each photon path[6]. However, the promise of this imaging modality lies in the fact that it affords new physical bases for contrast in tissue. For example, hemoglobin-based contrast in tumors relative to normal tissue is exceptionally high (i.e. between 100%-300%). However, improving the limitations associated with its low spatial resolution is fundamental to implementing this technology clinically. *A priori* knowledge of tissue structure can be used to constrain/guide the iterative NIR image reconstruction process, and improve the spatial resolution and quantitative accuracy of recovered physiological parameters. Consequently, NIR techniques have been combined with several high spatial-resolution, structure-bearing imaging modalities including x-ray tomosynthesis[7], ultrasound (US)[8], and magnetic resonance imaging (MRI)[9-11], to study human tissues and small animals. In this report, we present a combined NIR-MRI system for imaging female breast tissue, and explore the benefits of the combined data set in a planar tomographic geometry where the breast is imaged pendent in a standard MR breast coil.

In recent years, several important technological factors have contributed to the advancement of NIR spectral imaging applied to breast cancer characterization, including an increased understanding of light and tissue interaction, and new software-based developments in image-reconstruction algorithms for DOT[5]. NIR radiation (700-900 nm) is non-ionizing, light delivery and detection instrumentation is relatively inexpensive, and uncomfortable tissue compression is not required (as in mammographic level compression). NIR light transmission can typically be measured through as many as 12 cm of breast tissue depending on its composition and the wavelength of the NIR source. Photon propagation within the breast is well described by diffusion theory since the probability of photon scattering is much greater than absorption. Light transmission measurements can be combined with diffusion theory to provide robust image reconstruction of tissue optical coefficients. We use a Newton-type algorithm to solve for the optimal solution that provides a minimum error between the measured data and predicted response from a model of the frequency-domain diffusion equation[12]. Frequency-domain measurements contain information on both the amplitude change in the optical flux and time-based information. In theory, the approach allows separation of the absorption and reduced scattering coefficients (μ_a and μ_s') because the signal amplitude and phase shift provide a unique data set to solve the estimation problem associated with recovering both coefficients simultaneously.

A variety of imaging methods have achieved high-spatial-resolution imaging with acceptable to excellent soft tissue contrast, including X-ray computed tomography (CT), US, and MRI. These techniques primarily provide images of tissue structure and have a limited ability to monitor parameters related to tissue function other than through the introduction of exogeneous contrast agents. Alternatively, nuclear medicine approaches are routinely used to image tissue functions, such as metabolic fluorodeoxyglucose uptake[13], and many commercial systems exist to co-register these images with the structural data derived from CT, US and MRI. The combination of high resolution structural imaging with lower resolution functional information is a major emphasis in contemporary medical imaging, and customized hybrid imaging systems are being developed to avoid the complications associated with tissue movement between imaging exams, which compromises the accuracy of post-procedure co-registration.

The application of NIR tomography to provide spatially-resolved functional information, such as hemoglobin levels, oxygen saturation, water, lipid and scatterer content will likely be important, yet customized imaging systems which couple to MRI, US or CT need to be developed to evaluate and exploit this potential. The pioneering work of Ntziachristos *et al.*[10] was the first to demonstrate feasibility of the hybrid NIR-MR approach for clinical breast imaging. Their approach consisted of a co-planar array of optical source/sensors detecting time-resolved illuminations when applied to the surface of the breast. Data was presented as maps of localized optical response at each detector site but was otherwise not processed into depth-resolved images of optical property distributions. Zhu *et al.*[8] have demonstrated clinical application of a combined NIR-US system. With a hand-held probe, they simultaneously measure reflection of ultrasound and modulated NIR excitations at the breast tissue surface, and construct co-registered images of structure and optical absorption and hemoglobin concentration.

One of the most challenging issues in hybrid system development is the incorporation of anatomical information as prior constraints into NIR image reconstruction. This has been explored theoretically in several successful reports[14-19]. Structural information can be used to guide functional image reconstruction through knowledge of tissue composition and location by: (i) alteration of the objective functions used in image reconstruction[7, 20], (ii) reduction of the number of unknown parameters by treating regions of the same tissue type as single zones[10, 21], or (iii) introduction of special regularization schemes that can stabilize the inverse problem and emphasize image contrasts[7, 22, 23]. Optimizing spatial resolution more likely will depend on the application of all three techniques, while also being strongly influenced by the signal to noise ratio of the measurements, the optical contrast available, and the number of projections used. Some investigators have successfully combined different approaches with multi-stage image reconstruction algorithms[17, 18]. However, there is still no clear consensus on how best to utilize the structural information to enhance or improve the recovery of functional NIR information.

This work describes the first system to combine multi-spectral frequency-domain NIR in a planar tomographic geometry with MRI for imaging breast tissue. NIR tomography has shown the ability to localize changes in functional tissue parameters *in vivo*, and MRI has the advantage of offering a particularly rich amount of anatomical information, specifically about the layered adipose and glandular tissue structure of the breast. This system is designed to combine the benefits of both modalities into the construction of a single quantitative image. In particular, since NIR tomography has significant difficulty with the recovery of properties in layered structures, the initial information from MRI can significantly improve the estimation of breast properties, including in localized regions such as tumors.

The design and operation of the NIR-MRI system elements are described in Section II. The NIR component is similar to an imaging system described previously[24], which is currently being evaluated clinically, yet has the unique design feature of having no moving parts in the detection channels, allowing significant reduction in the NIR data acquisition time. In Section III we outline the theoretical basis, and the practical application and utilization of image reconstruction in NIR tomography. After applying several approaches to optimizing this hybrid reconstruction, an algorithm is examined that takes advantage of the composite data set. In

Section IV we discuss system performance and present images of phantom and breast optical properties which are both high resolution and quantitatively accurate.

II. SYSTEM DESIGN

This section describes the four elements that comprise the NIR-MRI system: (A) light delivery, (B) detector array, (C) fiberoptic patient interface, and (D) computer control and electronics. Element (C) extends from (A) and (B) into an MRI scanner for clinical studies, as shown schematically in Figure 1. Photographs of the rack-mounted system and patient interface are presented in Figure 2. Section (E) briefly describes phantom fabrication, and its importance in imaging system development and validation.

A. Light delivery

The system deploys six laser diodes: 661 nm (40 mW), 752 nm (50 mW), 785 nm (50 mW), 805 nm (50 mW), 829 nm (50 mW), and 849 nm (50 mW). Each wavelength is amplitude modulated at 100 MHz by mixing a DC current source (LDX-3220, ILX Lightwave, Bozeman, MT) and an AC current from a frequency generator (IFR-2023A, IFR Systems, Wilmington, MA), through a bias T (#5545, Picosecond Pulse Labs, Boulder, CO). Each diode is held in a laser tube (Thorlabs, Newton, NJ), and mounted on a linear translation stage (MA2515P5-S2.5 Velmex, Bloomfield, NY). This stage directs a specified wavelength into one of sixteen bifurcated optical fiber bundles which were custom designed for this application (Ceramoptec, East Longmeadow, MA). The 248-piece bundles (0.37 N.A., 0.68 packing fraction) are pure silica core (210 μm), silicone clad (230 μm) fibers suitable for transmission wavelengths from 400 nm to 2400 nm. The source light is delivered through the central seven fibers in each bundle, and the remaining fibers surrounding these are delivered to the detectors. The common end, which makes contact with the tissue, has a diameter of 4mm. Each fiber bundle is 13 meters in length and extends from the instrument cart, located outside of the MR suite, into the bore of the scanner (1.5T whole body imager, GE Medical Systems, Milwaukee, WI) to the patient interface. The efficiency of the optical switching is approximately 50%, yielding an average source power of 15 mW at the tissue surface.

B. Light detection

For each source excitation, light transmission is recorded from 15 surface locations. This signal is measured by 15 photomultiplier tubes (PMT R6357, Hamamatsu, Japan) operating in parallel. The gain of the PMTs is varied to account for the large variation in light level between detectors depending on their distance from the source. The gains are set by applying computer generated voltages between 0.4 and 1.2 V to their control lines, which sets the anode to cathode voltage between approximately 350 V to 1000 V, respectively. Using the higher gain settings, a PMT can reliably measure optical signals in the pW range. The optimal gain levels are determined prior to each imaging series. Each PMT is fixed to a particular fiber, so it is necessary to switch gains electronically during the course of data collection. A 100 MΩ resistor was used in the dynode chain of each PMT to achieve fast settling times after gain adjustment (200 ms for large gain changes). Electrical heterodyning through RF mixers (Minicircuits, Brooklyn, NY) is used to down convert the 100 MHz PMT signal to a lower frequency (500 kHz). This offset frequency is achieved with a second frequency-synthesizer which is synchronized to the one driving the laser current, and is set to 100.0005 MHz. The resulting offset frequency is filtered and amplified by a 16 channel circuit designed for this application (Audon Electronics, Nottingham, UK), then read by the computer. Lock-in detection is executed in software to extract amplitude and phase data for each of the detectors in parallel.

C. Fiberoptic patient interface

The MR exam is performed using a breast array coil (MRI Devices, Waukesha, WI) that offers high-resolution imaging. The coil also provides an open architecture, which allows for the integration of the NIR-breast interface shown in Figure 1. A circular ring machined from polyvinyl chloride (PVC) positions the common ends of the sixteen fibers around the full circumference of the pendant breast. Phosphor bronze compression springs (k=0.09lbs/in, Ace Wire Spring & Form, McKees Rocks, PA) guide each fiber through holes in the ring, into light contact with the tissue surface. The ring separates into equal halves so that it can easily be moved from one breast to the other. The angular separation between each fiber is 21 degrees, except between fibers adjacent to the line of ring devision, where the separation is 33 degrees. The ring can be positioned vertically, such that the plane of measurements intersects the region of interest in tissue. This design allows each fiber to move independently, therefore their radial positions may vary by several millimeters. In order to avoid serious artifacts in reconstructed images, the position of each fiber must be accurately known during data acquisition. Annular fiducial markers (MM 3005, IZI Medical Products, Baltimore, MD) are fixed to each fiber and can be located with sub-millimeter accuracy in the MRI.

D. Computer system

A PC running Labview software (National Instruments, Austin, TX) is used to control all light delivery and detection equipment. The laser current source and frequency generator parameters are set by a general purpose interface bus (GPIB, NI). The linear translation stage is addressed through the serial port. An analog output board (NI) is used for PMT gain control. A multipurpose data acquisition (DAQ) board acquires the 16 analog input channels and the single reference channel. This board also provides six digital output lines to the high power radio-frequency switch for the laser sources. For each source position, 15 signals from the detector system are amplified by a gain of 1000 and low pass filtered to prevent aliasing prior to the DAQ board using a 16 channel amplifier and filter network mounted in a BNC coupled box (Audon Electronics, Nottingham UK). Data are acquired for 500 ms, and phase and amplitude of each signal are calculated and written to file. Including the time required to determine optimal gain values, measurement with 6 wavelengths takes approximately 4 min. The MR exam is controlled separately, operated in parallel, and a full volume breast MRI is of similar duration. A FORTRAN, or MATLAB based reconstruction program reads and processes the NIR data[25-27]. MR images are processed off-line with an addition to the MATLAB software package, and incorporated into a modified iterative optical property reconstruction (see Section III).

E. Phantom Design

Tissue-simulating phantoms with known property distributions, geometries, and imaging orientations are commonly used to validate imaging systems. We have developed a recipe for producing gelatin materials with desired optical properties, and a shelf life of several months[28]. A heated mixture of water, gelatin (G2625, Sigma Inc.), India ink (for absorption), and titanium dioxide powder (for scatter) (TiO_2, Sigma Inc.) is poured into a mold of a desired shape, and solidified by cooling to room temperature. Variation in the water concentration provides MR contrast, and variable gel stiffness. The phantom imaged here (Section IV. B.) combines three gels with different optical properties in an irregular structure.

III. DATA PROCESSING AND IMAGE RECONSTRUCTION

Quantitative NIR imaging with model-based methods requires (A) important instrument calibration procedures, and (B) a reconstruction algorithm that incorporates an accurate model of light propagation in tissue.

A. System calibration

Calibration issues and other practical considerations associated with our NIR imaging approach have been discussed in detail elsewhere[26]. Two important procedures are briefly noted here: (1) detector calibration, and (2) homogeneous phantom calibration. First, the amplitude and phase response of each detection channel must be characterized in order to remove systematic noise in the data acquisition hardware. Each detector is exposed to the same optical signal, and the differences in log amplitude and phase are used as correction factors. The log amplitude response of the PMT is plotted against the log of the input power for each gain setting. A log—log regression is performed and the coefficients are used to calibrate detected PMT amplitude in terms of optical power. The phase does not fluctuate significantly with changing light level for a single gain setting (i.e. minimal phase-amplitude cross-talk), but is altered dramatically with changing gain. Relative phase differences between detectors are stored for calibration. These calibration curves are very similar to those created by McBride *et al*[24]. This characterization needs to be performed only once as long as the system is not modified.

The second important practical procedure is the correction for inter fiber variations and coupling issues, which is accomplished through a homogeneous phantom calibration process[26, 29]. This accounts for offsets due to optical fiber differences in transmission and alignment, as well as any errors in discretization or data-model mismatch. A homogeneous phantom is generally measured each day, and after system changes. The differences between data measured from the phantom, and data calculated from the model are stored and subtracted from measurements of the heterogeneous phantom or tissue under investigation. A homogeneous fitting algorithm is used to determine the μ_a and μ_s' values supplied to the model calculation. This algorithm can also be used to calculate the initial optical properties specified in iterative reconstruction of heterogeneous media. When dealing with tissues having arbitrary shape, the effectiveness of this fitting algorithm and homogeneous phantom calibration hinges on the accurate specification of source and detector locations. The ability to extract accurate fiber positions from MRI scans preserves the integrity of this method for non-uniform boundary data.

B. FEM analysis

Data acquired from the detection system is processed by a FEM based reconstruction algorithm to generate tomographic images of absorption and reduced scattering coefficients simultaneously. The algorithm exploits the frequency-domain diffusion equation approximation to light behavior in a highly scattering medium[25],

$$-\nabla \cdot D(\mathbf{r})\nabla\Phi(\mathbf{r},\omega)+\left(\mu_a(r)+\frac{i\omega}{c}\right)\Phi(\mathbf{r},\omega)=S(r,\omega) \tag{1}$$

where $S(r,\omega)$ is an isotropic light source at position r, $\Phi(\mathrm{r},\omega)$ is photon density at r, c is the speed of light in tissue, ω is the frequency of light modulation, μ_a is the absorption coefficient, and $D = \dfrac{1}{3(\mu_a + \mu_s^{/})}$ is the diffusion coefficient. The reduced (transport) scattering coefficient is given by $\mu_s^{/} = \mu_s(1-g)$, where g is the mean cosine of the single scatter function (the anisotropy factor), and μ_s is the scattering coefficient.

For a given μ_a and $\mu_s^{/}$ distribution, the diffusion equation is used to predict the optical flux at the detector sites for each source excitation. In the inverse problem (image reconstruction), the goal is the estimation of optical properties at each FEM node, based on measurements of optical flux at the detector sites on the tissue surface. This is achieved numerically by minimizing the difference between the calculated data Φ^C, and measured data, Φ^M, for all source/detector combinations (NM). Typically,

$$\chi^2 = \sum_{i=1}^{NM} \left(\Phi_i^C - \Phi_i^M\right)^2 \qquad (2)$$

is minimized in a least squares sense by setting the first derivative equal to zero, and using a Newton-Raphson approach to find the set of optical property values which approximate the point of stationarity. We use a Levenberg Marquardt algorithm, and repeatedly solve the equation

$$a = \left(J^T J + \lambda I\right)^{-1} J^T b, \qquad (3)$$

where $b = \left(\Phi^C - \Phi^M\right)^T$ is our data vector, and a is the solution update vector, $a = \lfloor \delta D_j ; \delta\mu_{aj} \rfloor$, defining the difference between the true and estimated optical properties at each reconstructed node j. Here, λ is a regularization factor to stabilize matrix inversion and J is the Jacobian matrix for our model, which is calculated using the Adjoint method[30].

Improving NIR reconstructions by incorporating MRI data have been explored in previous work[19, 20], and by other authors[10, 18, 21]. Techniques used to produce the images shown in Section IV include: (i) accurately defining the imaging volume, (ii) tailoring a regularization scheme which optimizes the reconstructed contrast of a suspicious area in the image, and (iii) reducing the number of unknown parameters by segmenting tissue types visible in the MRI. Defining the imaging volume, (i), is relatively straight forward and can be accomplished by creating a structured finite element mesh from the MRI. This mesh will often contain regional differences depending on tissue types present, and an irregular outer boundary due to impressions caused by fiber-tissue contact. In simulation studies, not presented here, it has been found that image reconstruction accuracy is easily degraded if the mesh (2D or 3D) does not represent the true outer tissue boundary. Step (ii) can be accomplished by changing λI in Eq. 3 to λA, where A is a regularization matrix, or filter matrix. Regularization can be thought of as a smoothing operator, where one can apply selective smoothing by linking together the property updates for all nodes associated with the same region or tissue type. Modifications to the Jacobian matrix size in a parameter reduction technique are used to implement step (iii)[20].

IV. PERFORMANCE AND EXPERIMENTAL RESULTS

In this section we (A) compare measurements from this system to those from a similar NIR tomography instrument described previously[24] for a number of tissue simulating phantoms. NIR-MRI phantom studies are described in (B), and *in vivo* images are shown in (C). For all results presented here, we used a single laser diode (785 nm) for convenience, and 2D modeling and image reconstruction. System performance and image quality at the other five wavelengths are comparable, and 3D imaging is readily achievable.

A. System performance

Measurement repeatability in terms of phase and log amplitude error was assessed by serially imaging a phantom with optical properties similar to those of average breast tissue (μ_a=0.004, $\mu_s^{/}$=1.35). The average RMS error at each detector site was determined to be 0.26% in ac intensity and 1.04° in phase. These values compare with those obtained from the system described by McBride *et al.* (0.32% in ac intensity and 0.48° in phase)[24]. RMS error for each of the 240 source-detector combinations for both systems is plotted versus PMT signal in Figure 3. For both phase and amplitude, error sharply increases when incident light falls below approximately 0.5 pW. These points are excluded in the calculation of average RMS error. As an additional comparison, we used both devices to measure a collection of phantoms (N=15) of varying diameters and optical properties. After processing the measurements with the homogeneous phantom calibration procedure described in Section III, we used the homogeneous fitting algorithm to determine a single μ_a and $\mu_s^{/}$ for each material. Table 1 shows the optical coefficients obtained with the NIR-MRI system, along with a measure of their discrepancy with those obtained with our stand-alone DOT instrumentation. We observed good agreement between the two systems. The absorption and scattering coefficients show correlation coefficients of R^2=0.984 and R^2=0.980, respectively.

B. Phantom Imaging

Due to the limited spatial resolution of DOT, layered media, small objects, and low contrast heterogeneity pose key challenges in image reconstruction. The capability of the presented system to address these challenges was investigated by imaging a phantom comprised of three gels with different optical properties. The phantom is cylindrical and the boundary between the outer layer and inner layer is irregular. A two centimeter spherical inclusion is embedded within the inner layer. The optical coefficients of each gel are known (Table 2), as each material was created using a practiced recipe to give desired values. Furthermore, the true value of each layer was validated by creating a separate homogenous phantom for each layer (at the same time as creating layered phantom) and measuring bulk properties with a homogeneous fitting algorithm. To increase MRI contrast between layers, Omniscan™ (gadodiamide) was added to the inner layer (0.005 g/ml).

A photograph of the phantom, alongside another spherical inclusion is shown in Figure 4(a). Figure 4(b) shows a T1-weighted, gradient echo MRI (25 ms TR, 3 ms TE, 45^0 flip angle) cross-section of the phantom in the plane of the optical fibers. This was used to create a 2D structured finite element mesh and to locate the positions of the 16 fibers (Figure 4(c)). Fiber fiducials were not used in this experiment, but the 16 impressions caused by each optical fiber are clearly visible around the perimeter of the gel. Each of the three regions are also visible, corresponding to each of the three types of optically variant gel. 3D meshing and imaging is also possible, given that a stack of MR slices represent the full volume structure of the phantom. The system design allows for NIR data acquisition in multiple planes if desired.

Using log amplitude and phase data, images of optical properties were reconstructed with two different algorithms. The first algorithm solves Eq. (3) without *a priori* guidance, except for the use of the mesh and source locations from Figure 4(c). The corresponding reconstructed images are presented in Figure 5(a). The second algorithm uses the layered structure from the MRI to constrain Eq. (3). The regularization parameter associated with each reconstructed node is adjusted based upon its location and area of influence. Lower values are used for small regions close to the center of the reconstructed volume, whereas peripheral regions (which are prone to large artifacts) have larger regularization. A regularization matrix (*A*), or filter matrix, based upon the *a priori* structural information from the MRI was also used to further improve the algorithm. The optimal values for λ and *A* were determined in simulation studies of this geometry, using similar contrast and noise levels. These can also be chosen automatically once an empirical knowledge of their effect is established. The images reconstructed from this modified constrained algorithm are shown in Figure 5(b).

Qualitatively, the algorithm that uses MRI information to guide the iterative process performs much better. The optical property images in Figure 5(a) are blurry and "edge artifacts" are clearly visible, especially for μ_s'. The absorbing sphere near the center of the phantom is recovered with poor spatial resolution, and its contrast is underestimated. The property maps in Figure 5(b) have improved resolution. Spatial resolution and contrast of the spherical inclusion are better. As a quantitative measure of the accuracy of image reconstruction, we compute the RMS error between the target image and the reconstructions, node by node. This measure indicates a dramatic improvement for the second method [RMS(μ_a)=0.0024, RMS(μ_s')=0.19] relative to the first [RMS(μ_a)=0.0034, RMS(μ_s')=0.25].

C. *In Vivo* Imaging

The Institutional Review Board (IRB) at the Dartmouth Hitchcock Medical Center approved this clinical examination protocol, and written informed consent was obtained from all volunteering women. Figure 6 (a and b) show a photograph of a subject lying on the examination platform, and an anatomical axial MR image through the breast. NIR measurements (4 wavelengths in this case) and a full volume MRI (50 coronal slices, 25 ms TR, 6 ms TE, 45^0 flip angle, 2 mm slice thickness) were obtained in less than 10 minutes. Figure 7(a) shows an anatomically coronal MRI with 16 fiducial-marked fibers (appearing as bright white spots outside the breast). The radiographic density of this participant is heterogeneously dense (HD), and a large interior region of glandular tissue is easily defined in the FEM mesh shown in Figure 7(b).

As with the phantom study, we present images of μ_a and μ_s' at 785nm reconstructed with two different algorithms. The first result, obtained by solving Eq. (3), without *a priori* guidance, is shown in Figure 7(c). As expected, we see higher absorption and scatter in the glandular region (central) relative to the adipose tissue (peripheral). However, the region of increase does not span the full area expected, and heterogeneity is visible (especially around the perimeter of the image. The second algorithm assumes homogeneous optical properties for each tissue type, and utilizes parameter reduction[20], which leads to a 'fitting' for four values: $\mu_{a\ adipose}$=0.003, $\mu_{s\ adipose}'$=0.93, $\mu_{a\ glandular}$=0.006, $\mu_{s\ glandular}'$=1.12 (Figure 7(d)). This algorithm is robust to noise and converges after a few iterations. The result is quantitatively logical, and similar values are recovered using spatially varying regularization (as described in the phantom reconstruction).

V. DISCUSSION AND CONCLUSION

This article describes a novel *in vivo* breast imaging system that synergistically combines NIR tomography with MRI. Tissue structures visible with high resolution in MRI can be applied *a priori* to optical property reconstructions from frequency-domain NIR measurements. Thus, the reconstruction process can be optimized to produce high resolution, quantitatively accurate maps of absorption and reduced scattering coefficients, and ultimately physiologically relevant parameters. Various physiological tissue types exhibit significant contrast in the NIR, primarily though, the combined system could be very effective at locating and diagnosing breast tumors.

The NIR component provides multi-spectral (6 wavelengths) frequency-domain (log amplitude and phase) data from 16 fiber-tissue contact positions around the breast's circumference. Data acquisition is fully automated, and a complete set of measurements (240 source-detector pairs) for one wavelength requires approximately 40 s. Light detection is highly sensitive (subpicowatt limit) with low noise (RMS <0.26%, <1.04° in phase). All optical elements and controls are mounted in a portable cart, and operation inside strong magnetic fields is facilitated with long optical fibers and an easy-to-use positioning system/patient interface.

The deployment of dual modality NIR imaging systems in clinical applications has been limited to date, mainly because of the complexity of the image reconstruction problem. Here, a representative phantom and *in vivo* study using one wavelength (785 nm) are presented. We have shown that co-registered MRI validates and improves optical property estimation in 2D tomographic image reconstructions when specialized algorithms are used. Future work will involve 3D modeling and reconstruction, which could further improve both qualitative and quantitative aspects of the recovered coefficient values.

Preliminary results are encouraging, and have allowed us to optimize reconstruction techniques, and automate constraint selection. We have performed several phantom studies, and demonstrated the feasibility of imaging volunteers with healthy breasts. Through the study of more healthy subjects, with different radiographic densities, we aim to compare functional parameters of adipose versus glandular tissue. To test the system's ability at diagnosing tumors, cancer patients will be recruited, and the simultaneous exam will likely involve MR contrast enhancement.

VI. Acknowledgements

The authors would like to express sincere gratitude to Gordon Ehret and Richard Johnson for their fine fabrication work. This work has been sponsored by the National Cancer Institute through grants RO1CA78734, PO1CA80139, and DAMD17-03-1-0404.

VII. References

[1] V. Ntziachristos, A. H. Hielscher, A. G. Yodh, and B. Chance, IEEE transactions on medical imaging **20**, 470 (2001).

[2] B. W. Pogue, S. P. Poplack, T. O. McBride, W. A. Wells, O. K. S, U. L. Osterberg, and K. D. Paulsen, Radiology **218**, 261 (2001).

[3] S. Srinivasan, B. W. Pogue, S. Jiang, H. Dehghani, C. Kogel, S. Soho, J. J. Gibson, T. D. Tosteson, S. P. Poplack, and K. D. Paulsen, Proc. Nat. Acad. Sci. **100**, 12349 (2003).

[4] B. J. Tromberg, N. Shah, R. Lanning, A. Cerussi, J. Espinoza, T. Pham, L. Svaasand, and J. Butler, Neoplasia **2**, 26 (2000).

[5] S. R. Arridge, Inverse Problems **15**, R41 (1999).

[6] H. Dehghani, B. W. Pogue, S. Jiang, B. A. Brooksby, and K. D. Paulsen, Applied Optics **42**, 3117 (2003).
[7] A. Li, E. L. Miller, M. E. Kilmer, T. J. Brukilaccio, T. Chaves, J. Stott, Q. Zhang, T. Wu, M. Choriton, R. H. Moore, D. B. Kopans, and D. A. Boas, Applied Optics **42**, 5181 (2003).
[8] Q. Zhu, N. G. Chen, and S. H. Kurtzman, Optics Letters **28**, 337 (2003).
[9] B. W. Pogue, H. Zhu, C. Nwaigwe, T. O. McBride, U. L. Osterberg, K. D. Paulsen, and J. F. Dunn, Oxygen Transport to Tissue XXIV, 215 (2002).
[10] V. Ntziachristos, A. G. Yodh, M. D. Schnall, and B. Chance, Neoplasia **4**, 347 (2002).
[11] G. Gulsen, H. Yu, J. Wang, O. Nalcioglu, S. Merritt, F. Bevilacqua, A. J. Durkin, D. J. Cuccia, R. Lanning, and B. J. Tromberg, Technology in Cancer Research & Treatment **1**, 1 (2002).
[12] K. D. Paulsen, and Jiang H., Med. Phys. **22**, 691 (1995).
[13] M. Tatsumi, C. Cohade, Y. Nakamoto, and R. L. Wahl, Radiology **229**, 831 (2003).
[14] R. L. Barbour, H. L. Graber, J. Chang, S. S. Barbour, P. C. Koo, and R. Aronson, IEEE Comp. Sci. Eng. **2**, 63 (1995).
[15] A. H. Barnett, J. P. Culver, A. G. Sorensen, A. Dale, and D. A. Boas, Appl. Opt. **42**, 3095 (2003).
[16] V. Ntziachristos, X. H. Ma, and B. Chance, Review of Scientific Instruments **69**, 4221 (1998).
[17] M. Torregrossa, C. V. Zint, and P. Poulet, Optical Tomography and Spectroscopy of Tissue V (2003).
[18] M. Schweiger and S. R. Arridge, Physics in Medicine and Biology **44**, 2703 (1999).
[19] B. W. Pogue, T. O. McBride, C. Nwaigwe, U. L. Osterberg, J. F. Dunn, and K. D. Paulsen, SPIE Conference **SPIE volume 3597**, 484 (1999).
[20] B. A. Brooksby, H. Dehghani, B. W. Pogue, and K. D. Paulsen, IEEE JSTQE **9**, 199 (2003).
[21] N. G. Chen, P. Guo, S. Yan, D. Piao, and Q. Zhu, Applied Optics **40**, 6367 (2001).
[22] B. W. Pogue, McBride, T. O., Prewitt, J., Osterberg, U. L., Paulsen, K. D., Appl. Opt. **38**, 2950 (1999).
[23] M. Belge, M. E. Kilmer, and E. L. Miller, Inverse Problems **18**, 1161 (2002).
[24] T. O. McBride, B. W. Pogue, S. Jiang, U. L. Osterberg, and K. D. Paulsen, Review of Scientific Instruments **72**, 1817 (2001).
[25] H. Dehghani, B. W. Pogue, S. P. Poplack, and K. D. Paulsen, Applied Optics **42**, 135 (2003).
[26] T. O. McBride, B. W. Pogue, U. L. Osterberg, and K. D. Paulsen, Oxygen Transport to Tissue XXIV, 85 (2002).
[27] B. W. Pogue, S. Geimer, T. O. McBride, S. Jiang, U. L. Osterberg, and K. D. Paulsen, Applied Optics **40**, 588 (2001).
[28] D. Li, P. M. Meany, T. D. Tosteson, S. Jiang, T. Kerner, T. O. McBride, B. W. Pogue, A. Hartov, and K. D. Paulsen, Medical Physics **30**, 2194 (2003).
[29] S. Jiang, B. W. Pogue, T. O. McBride, M. M. Doyley, S. P. Poplack, and K. D. Paulsen, Journal of Electronic Imaging **12**, 613 (2003).
[30] S. R. Arridge and M. Schweiger, Appl. Opt. **34**, 8026 (1995).

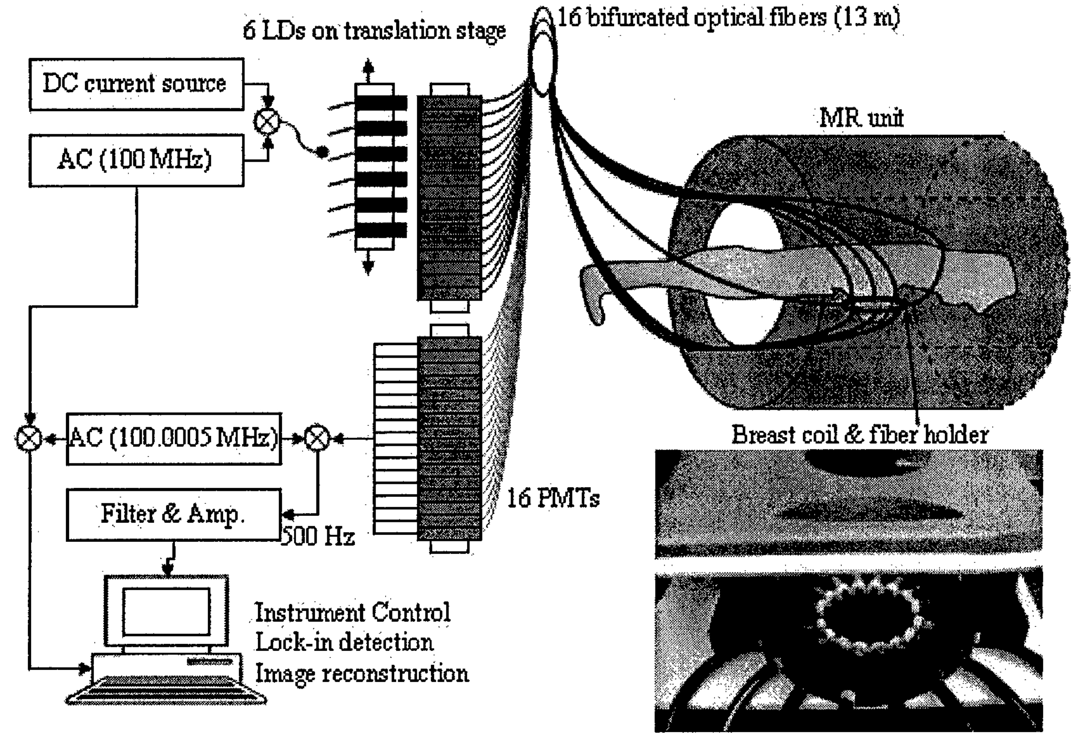
6 LDs on translation stage
16 bifurcated optical fibers (13 m)
DC current source
AC (100 MHz)
MR unit
AC (100.0005 MHz)
Breast coil & fiber holder
Filter & Amp.
500 Hz
16 PMTs
Instrument Control
Lock-in detection
Image reconstruction

Figure 1. Schematic design of a dual modality NIR-MRI system (left). Frequency-domain NIR tomography is performed inside the MRI unit (upper right). Six laser diodes (660-850nm) are amplitude modulated, and sixteen projections yield 240 measurements of amplitude and phase of transmitted light. The fiber optic array is positioned inside the open breast coil, to allow positioning along the length of the pendant breast (bottom right).

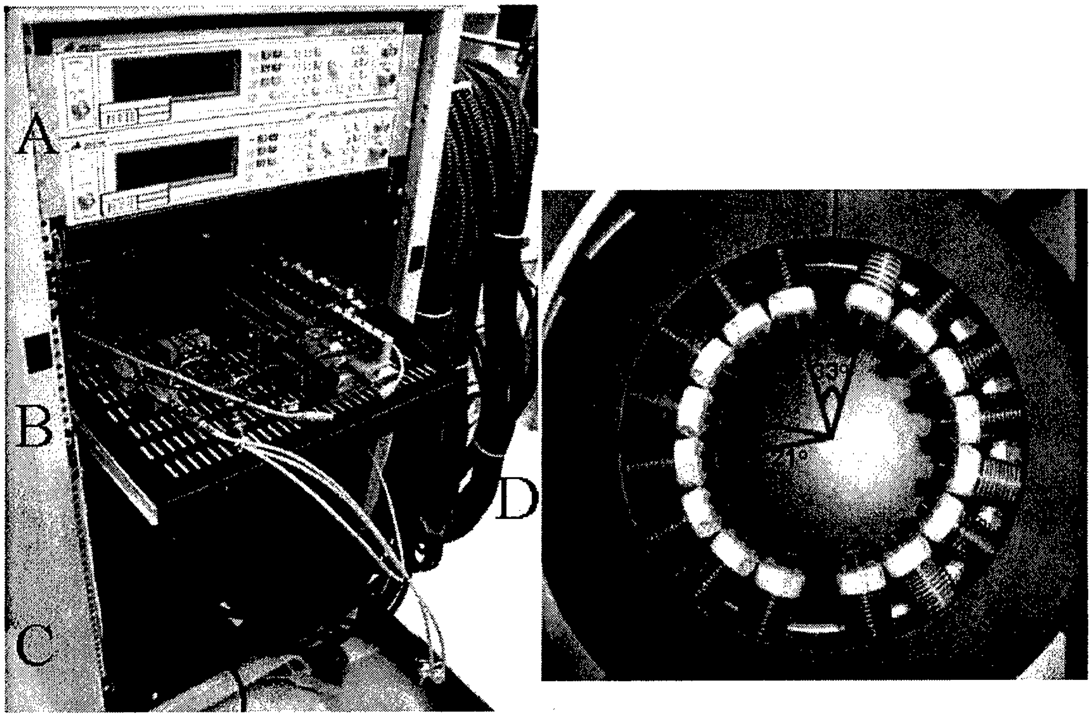

Figure 2. Photograph of the rack mounted, portable system (left). System components are marked, including (A) frequency generators, (B) optical switching stage, (C) PMT detection plate, and (D) optical fibers and patient interface. The fiber-patient interface (at right) can accommodate breasts 6-12 cm in diameter. A close up of the tissue coupling system shows that the fibers are spring-loaded and make light contact with the full circumference of a pendant breast.

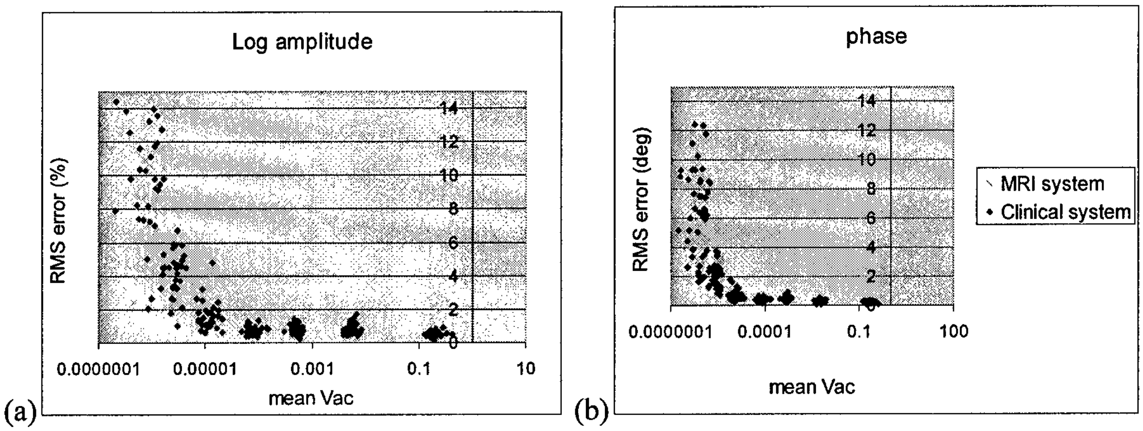

Figure 3. Repeatability assessment for (a) log amplitude and (b) phase of NIR component of combined NIR-MRI system and stand-alone NIR tomography system at Dartmouth. The performance of the two systems is comparable. In routine operation, PMT voltage signals are above 1.0 x 10^{-5} V.

	μ_a (mm^{-1}) (NIR-MRI)	% difference	μ_s' (mm^{-1}) (NIR-MRI)	% difference
Mean	0.0055	-6.2	1.34	9.1
Max	0.0102	6.3	1.91	29.6
Std. Dev.	0.0024	8.7	0.41	7.9

Table 1. Optical properties at 785nm for 15 tissue simulating phantoms, and % differences from values determined using another NIR tomography system.

	Outer Layer	Inner Layer	Inclusion
μ_a (mm^{-1})	0.0044	0.0062	0.02
μ_s' (mm^{-1})	0.51	0.68	0.9

Table 2. Approximate optical properties of gelatin phantom.

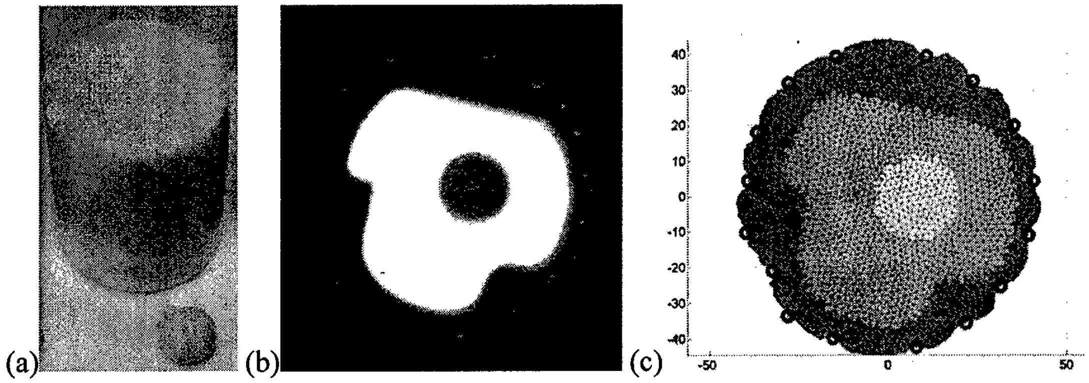

Figure 4. (a) The gelatin phantom. (b) T1-weighted MRI image of the structure of the phantom cross-section. The inner layer (light region) contains gadodiamide for MR contrast (0.005 g/ml). The inner inclusion is a 2 cm diameter sphere. (c) Finite element mesh derived from the three-layered structure image in (b). The circles on the outer boundary indicate the fiber locations. Axes are in millimeters.

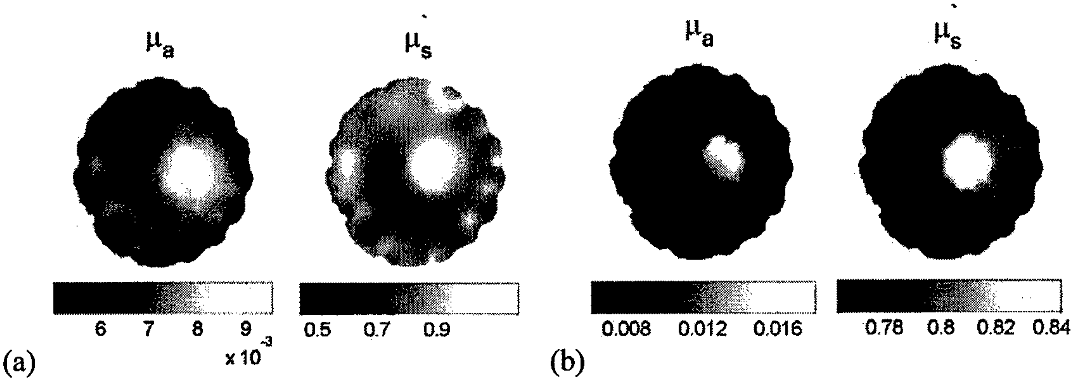

Figure 5. Images in (a) show optical property reconstructions without MRI guidance. In (b), reconstructions improve when the interior structural information of the MRI is incorporated. Comparing these two images, the latter has a reduction in artifacts in the reduced scattering image, and both the spatial resolution and contrast have improved. The recovered values compare favorably with the approximate true values shown in Table 2.

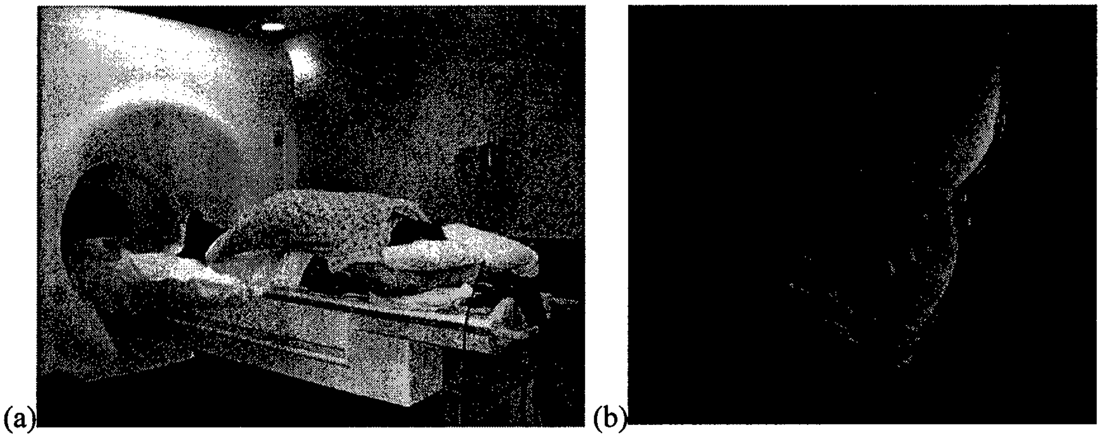

Figure 6. Photograph in (a) shows a female volunteer prepared for the simultaneous MRI-NIR exam. In an anatomically axial T1-weighted MRI slice from the right breast, (b), fiducial markers (outside the breast) indicate the location of the fiber plane.

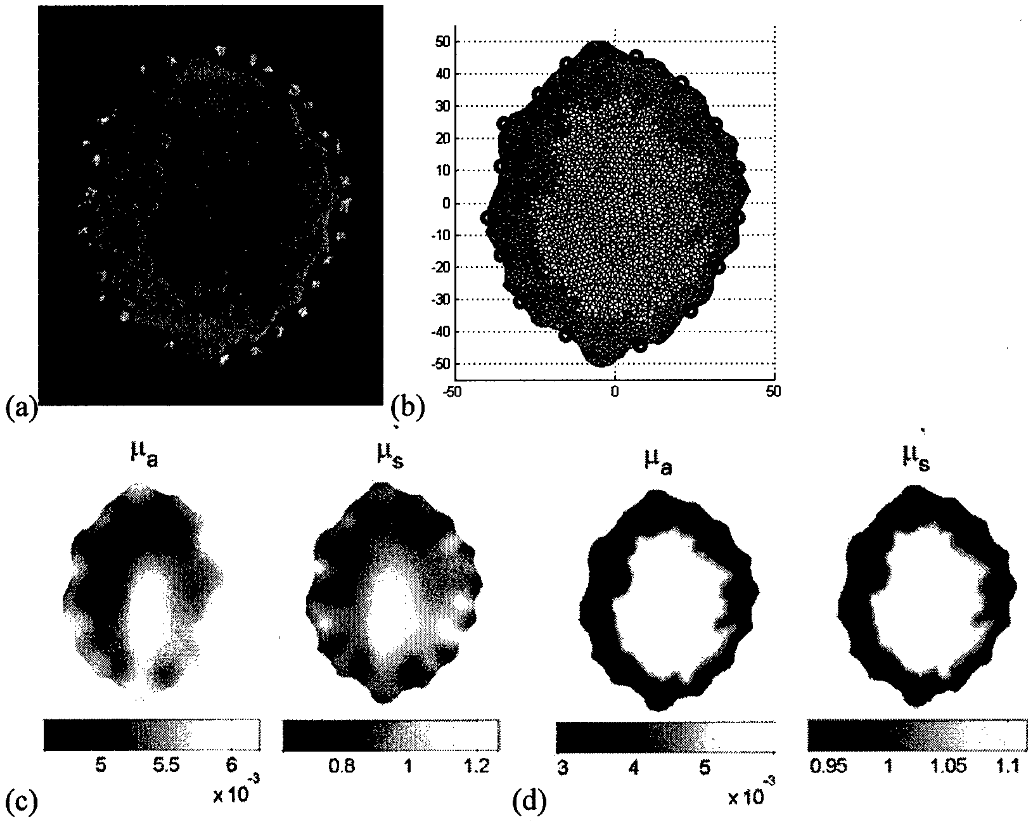
(a)
(b)
50
40
30
20
10
0
-10
-20
-30
-40
-50
-50
0
50
μ_a
μ_s
μ_a
μ_s
5
5.5
6
x 10^{-3}
0.8
1
1.2
3
4
5
x 10^{-3}
0.95
1
1.05
1.1
(c)
(d)

Figure 7. In (a), an anatomically coronal T1-weighted MRI displays adipose (outer) and glandular (inner) tissue types. A two layer structured FEM mesh and source locations, created from (a), is shown in (b). Optical property reconstructions in (c) are obtained without utilizing the internal structure of (b). In (d), MRI data guides a two-region parameter fitting algorithm. This result is improved relative to (c), and shows increased absorption and scatter in glandular relative to adipose tissue.